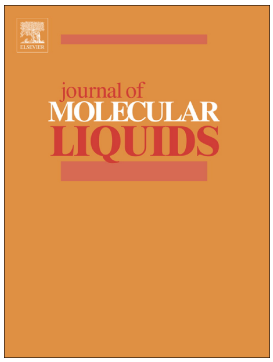

Ca-alginate/carboxymethyl chitosan/Ni0.2Zn0.2Fe2.6O4 magnetic bionanocomposite: Synthesis, characterization and application for single adsorption of Nd+3, Tb+3, and Dy+3 rare earth elements from aqueous media

Hamedreza Javadian, Montserrat Ruiz, Tawfik A. Saleh, Ana Maria Sastre

PII: S0167-7322(19)36443-8

DOI: https://doi.org/10.1016/j.molliq.2020.112760

Reference: MOLLIQ 112760

To appear in: *Journal of Molecular Liquids*

Received date: 22 November 2019

Revised date: 18 February 2020

Accepted date: 20 February 2020

Please cite this article as: H. Javadian, M. Ruiz, T.A. Saleh, et al., Ca-alginate/carboxymethyl chitosan/Ni0.2Zn0.2Fe2.6O4 magnetic bionanocomposite: Synthesis, characterization and application for single adsorption of Nd+3, Tb+3, and Dy+3 rare earth elements from aqueous media, *Journal of Molecular Liquids*(2018), https://doi.org/10.1016/j.molliq.2020.112760

Ca-alginate/carboxymethyl chitosan/$Ni_{0.2}Zn_{0.2}Fe_{2.6}O_4$ magnetic bionanocomposite: Synthesis, characterization and application for single adsorption of Nd^{+3}, Tb^{+3}, and Dy^{+3} rare earth elements from aqueous media

Hamedreza Javadian[a,*], Montserrat Ruiz[b], Tawfik A. Saleh [c,*], Ana Maria Sastre[a]

[a]Department of Chemical Engineering, ETSEIB, Universitat Politècnica de Catalunya, Diagonal 647, 08028 Barcelona, Spain

[b]Department of Chemical Engineering, EPSEVG, Universitat Politècnica de Catalunya, Av. Víctor Balaguer, s/n, 08800 Vilanova i la Geltrú, Spain

[c]Chemistry Department, King Fahd University of Petroleum and Minerals, Dhahran 31261, Saudi Arabia

[*]Corresponding author.

Email addresses: hamedreza.javadian@yahoo.com, hamedreza.javadian@upc.edu (H. Javadian); tawfikas@hotmail.com (T Saleh)

Abstract

This study aims to research the adsorption of Nd^{+3}, Tb^{+3}, and Dy^{+3} from aqueous media onto the magnetic calcium alginate/carboxymethyl chitosan/$Ni_{0.2}Zn_{0.2}Fe_{2.6}O_4$ (CA/CMC/$Ni_{0.2}Zn_{0.2}Fe_{2.6}O_4$) bionanocomposite in a single system. FE-SEM, FT-IR, EDX, VSM, and TGA were applied to characterize the product. The VSM result showed the saturation magnetization values of 45.87 and 14.14 emu/g for the bare $Ni_{0.2}Zn_{0.2}Fe_{2.6}O_4$ nanoparticles and CA/CMC/$Ni_{0.2}Zn_{0.2}Fe_{2.6}O_4$, respectively. The adsorption results showed that at optimum conditions of contact time of 40 min, pH of 5.5, and 0.8 g/L, the adsorption efficiency of the adsorbent for Nd^{+3}, Tb^{+3}, and Dy^{+3} was 97.75, 96.83, and 97.85 %, respectively. The ions adsorption kinetic onto the CA/CMC/$Ni_{0.2}Zn_{0.2}Fe_{2.6}O_4$ was in accordance with pseudo-second-

order (PSO) model. The evaluation of equilibrium data was performed by the isotherm models of Langmuir and Freundlich. Fitting the experimental data of Tb^{+3} and Dy^{+3} was done better with Freunlich model than Langmuir model, while fitting tests for Nd^{+3} adsorption data showed better coverage using Langmuir model with a maximum adsorption capacity of 73.37 mg/g. The results of the parameters of thermodynamic showed the endothermic and spontaneous properties of the process. Additionally, the efficacy of the adsorbent was studied using 0.2 M HNO_3 in four adsorptions–desorption cycles. Overall, the obtained results demonstrated that the environmentally friendly magnetic bionanocomposite adsorbent can be applied effectively for Nd^{+3}, Tb^{+3}, and Dy^{+3} adsorption with favorable adsorption efficiency.

Keywords: Carboxymethyl chitosan; Calcium alginate; $Ni_{0.2}Zn_{0.2}Fe_{2.6}O_4$; Adsorption; Rare earth elements

1. Introduction

Rare earth elements (REEs) are getting impressive considerations and progressively requested in innovative industries in view of their novel properties [1]. As of late, they have been discovered broad demands in batteries, electronics, and chemical engineering [2,3]. Because of enormous and expanding local requests, China reduced its amount of REEs send out from 50145 tons in 2009 to just 31130 tons in 2012. These fare quantities may create difficult issues for REE applicants outside of China, as proved by the crisis of REEs in 2011, recording high costs of these elements [4]. This circumstance has additionally animated many nations, for example, Japan and most EU Member States that don't have any sort of essential REEs stores on their region to search for option and auxiliary resources of REEs and to extend their own REEs industry so as to get a wellspring of REEs, especially heavy REEs [5]. In this manner, a productive method is expected to overcome all difficult issues with respect to REEs.

The conventional methodologies applied for REEs recovery are chemical precipitation, membrane separation, ion-exchange, reverse osmosis, extraction, and adsorption [6-8]. However, each method has its advantages and disadvantages. For instance, chemical precipitation has the advantage of low-cost and simple operation, but large amounts of chemical products are produced, resulting in landfill problems [9]. Membrane separation method has the advantages of high separation efficiency for heavy metal ions, yet low economic feasibility and high maintenance cost restrict its application on a large scale. Adsorption technology, which is easy to perform, highly effective, and low-cost, is considered as a fast and relatively inexpensive approach for metal ions adsorption [10]. Adsorption of REEs has been investigated by some materials such as biosorbents [11-13], carbon [14,15], silica other inorganic [16, 17,18], and polymeric materials [19,20].

Alginate, as a valuable natural polymer, has pulled in extreme consideration. It is an ordinary polysaccharide that is made up of the residues of mannuronic (M) and guluronic (G) acid (linear copolymer of β-D-mannuronic acid and α-L-guluronic acid units with (1-4) linkages) [21]. This environmentally friendly polymer has highlights of cheapness, plentiful sources, biocompatibility, and hydrophilicity. More often than not, industrially accessible alginates are extraction of brown algae cell wall [22]. It has been broadly utilized in immobilization studies owing to easy preparation, hydrophilicity and efficient adsorption of target contaminations.

Chitosan (CS) as a natural polysaccharide is generally made using the deacetylation of chitin. Its derivatives can be generated by the functional groups' modification, for instance, reactive hydroxyl, amino, and N-acetyl groups [23]. Carboxymethyl chitosan (CMC) is considered as the most significant derivatives amongst others. It is the result of the carboxylation of chitosan that has carboxymethyl substituents on amino and hydroxyl groups of the

glucosamine units [24]. Because of having special characteristics such as nontoxicity, hydrophilicity, biodegradability, environmentally friendly, and metal-chelating capacity, it is viewed as a potential candidate for bioadsorption. Nevertheless, it couldn't be used for the recovery of ions because of being water-dissolvable and having weak chemical stability [25]. So as to defeat this issue, modification of CMC by other biopolymers such as alginate and inorganic nanoparticles can be regarded as one of the best techniques to increase its hydrolysis resistance.

The purpose of this study was to synthesize the $Ni_{0.2}Zn_{0.2}Fe_{2.6}O_4$ magnetic nanoparticles by the hydrothermal technique and using the synthesized nanoparticles for the synthesis of a bionanocomposite in gelation process of sodium alginate and carboxymethyl chitosan biopolymers in a medium of $CaCl_2$ and glutaraldehyde. After characterizing the product with various techniques including FE-SEM, EDX, XRD, FT-IR, and VSM, it was used as an adsorbent to investigate the adsorption efficiency of Nd^{+3}, Tb^{+3}, and Dy^{+3} depending on adsorbent dosage, pH, contact time, initial metal ion concentration by performing a series of batch experiments. Various kinetic and isotherm models were tested for fitting the experimental data. Thermodynamic parameters (ΔS°, ΔG°, and ΔH°) were also evaluated to find the property of adsorption process. To the best of our knowledge, the utilization of the CA/CMC/$Ni_{0.2}Zn_{0.2}Fe_{2.6}O_4$ has not been studied for Nd^{+3}, Tb^{+3}, and Dy^{+3} adsorption.

2. Materials and methods

2.1. Materials and reagents

Carboxymethyl chitosan and sodium alginate were purchased from Nantong Chem-Base Co, China, and PanReac AppliChem, respectively. $Nd(NO_3)_3.6H_2O$, $Tb(NO_3)_3 \cdot 6H_2O$, $Dy(NO_3).5H_2O$, $Zn(NO_3)_2$, $Fe(NO_3)_3.6H_2O$, $Ni(NO_3)_2 \cdot 6H_2O$, and glutaraldehyde were bought from Sigma-Aldrich. Since the analytical grade of all chemicals was chosen, they were utilized

without further purification. The experiment solutions of Nd^{+3}, Tb^{+3}, and Dy^{+3} were prepared by dilution of 1000 mg/L of ions. The values of pH were regulated via adding a suitable amount of 0.1 M sodium hydroxide or nitric acid solutions and monitored by a pH meter.

2.2. Instrumentation and characterization

FT-IR spectra were recorded on a PerkinElmer, USA, by KBr pellet. XRD pattern was recorded by a GBC MMA instrument with CuK_α radiation in the 2θ range of 10–70° . A FE-SEM (Zeiss Neon-40, Germany) was also utilized for characterizing the products morphology. The magnetic properties of the products were explored at the room temperature (RT) by employing a VSM (Daghigh Kavir Corporation, Iran). TGA was done on a Mettler TGA/SDTA 851e/LF/1100 thermobalance. The temperature of the sample was increased from RT to 1000 °C (rate=10 °C/min) under constant nitrogen flow. For analyzing Nd^{+3}, Tb^{+3}, and Dy^{+3} concentration, an Agilent 4100 MP-AES Spectrometer was used.

2.3. Synthesis of the $Ni_{0.2}Zn_{0.2}Fe_{2.6}O_4$ magnetic nanoparticles

The $Ni_{0.2}Zn_{0.2}Fe_{2.6}O_4$ magnetic nanoparticles were synthesized by the hydrothermal method. A mixed solution of 0.2 M Ni^{2+}, 0.2 M Zn^{2+} and 2.6 M Fe^{3+} was prepared in HCl solution, and then NaOH solution was introduced under nitrogen gas and the value of the pH of the mixture was regulated to 10.5. To this mixture, 0.3 g of CTAB was added, and then it was placed into an autoclave (Teflon-lined stainless steel) at 200 °C of an oven for 8 h for hydrothermal treatment. In the following, the temperature of the autoclave was naturally decreased to RT. The precipitate was then collected and washed with deionized water **(**DW) several times to reach pH=7. Finally, the obtained particles were dried at 50 °C.

2.4. Synthesis of the CA/CMC/$Ni_{0.2}Zn_{0.2}Fe_{2.6}O_4$ magnetic bionanocomposite

The synthesis procedure of the CA/CMC/$Ni_{0.2}Zn_{0.2}Fe_{2.6}O_4$ was as follows: Sodium alginate (1 g) was dissolved in 80 mL of DW at RT by a laboratory stirrer. 0.50 g of the carboxymethyl chitosan was introduced into the solution and homogeneously mixed. 0.7 g of the $Ni_{0.2}Zn_{0.2}Fe_{2.6}O_4$ was added to the mixture of the biopolymers. To obtain a homogeneous blend solution, the mixture of biopolymers and magnetic particles was stirred at the RT for 24 h. In the following, it was added into the solution of calcium chloride 0.05 M and 2 % glutaraldehyde for gelation process. After the completion of gelation process, an external magnetic field was utilized for the separation of the resulting bionanocomposite, and then it was washed using DW several times to eliminate any remaining calcium chloride and glutaraldehyde until the pH of the solution reached 7. The washed CA/CMC/$Ni_{0.2}Zn_{0.2}Fe_{2.6}O_4$ bionanocomposite was dried at 50 $^{\circ}$C. Finally, it was powdered.

2.5. Batch adsorption and reusability studies

The stock solutions of metal ions were prepared by dissolving $Tb(NO_3)_3 \cdot 6H_2O$, $Nd(NO_3)_3.6H_2O$, and $Dy(NO_3).5H_2O$ separately in DW to achieve 1000 mg/L of each ion, and all the experiment solutions containing 50 mL of single ion prepared by dilution of each stock solution to the required concentration were agitated at 180 rpm by a laboratory shaker. Equal concentration of the ions was applied in single batch adsorption studies. For studying the influences of pH and adsorbent dosage on the ions adsorption efficiency, batch adsorption experiments were performed in the pH range of 1.5-5.5 and dosage range of 0.01-0.06 g, respectively. For the kinetic evaluation, the adsorbent was added into the solutions with 30 mg/L initial concentration, and the tests were performed at different contact time (2.5-70 min). Initial metal concentration in the range of 30-300 mg/L at the optimum time was used to investigate the isotherm of the adsorption. The effect of ionic strength was studied with $NaNO_3$ solution at various

concentrations of 0.02, 0.04, 0.06, 0.08, and 0.1 M. To evaluate thermodynamic parameters, the experiments were carried out at three various temperatures of 25, 35 and 45 °C at a constant initial concentration of 90 mg/L. The ions concentration in the solution was measured by an Agilent 4100 MP-AES Spectrometer. The adsorption efficiency (%) and capacity of metal adsorption by the CA/CMC/$Ni_{0.2}Zn_{0.2}Fe_{2.6}O_4$ were computed using the equations in the following:

$$\text{Adsorption efficiency (\%)} = (C_0 - C_e)/C_o \times 100 \quad (1)$$

$$q_e = (C_0 - C_e) \times V/m \quad (2)$$

$$q_t = (C_0 - C_t) \times V/m \quad (3)$$

Where the q_e and q_t (mg/g) refer to the quantities of metal ion adsorbed at equilibrium and adsorption time t in min, respectively. C_0 and C_e show the initial and equilibrium concentrations of metal ion in mg/L, respectively. C_t refers to the concentration of a metal ion in solution at time t (min). Moreover, m refers to the adsorbent weight (g), and V refers to the solution volume in L.

To investigate the reusability of the CA/CMC/$Ni_{0.2}Zn_{0.2}Fe_{2.6}O_4$, a given amount of the adsorbent was treated with 50 mL of 30 mg/L metal solution at pH of 5.5 by a shaker at speed of 180 rpm to obtain the exhausted adsorbent. The ions-loaded adsorbent was separated with an external magnetic field, washed by DW to eliminate the un-adsorbed ions and then agitated for 2 h by 50 mL HNO_3 (0.2 M) eluent solution. Subsequently, the regenerated CA/CMC/$Ni_{0.2}Zn_{0.2}Fe_{2.6}O_4$ was separated and washed several times with DW until the solution pH reached 7. The regenerated adsorbent was applied in four cycles of adsorption with the same regeneration procedure.

3. Results and discussion

3.1. Analyses of the products

Fig. 1 indicates the XRD pattern of the $Ni_{0.2}Zn_{0.2}Fe_{2.6}O_4$. The peaks at $2\theta = 18.13^{\circ}$, 30.07°, 35.50°, 37.08°, 43.07°, 53.95°, 56.96°, and 63.89° are in agreement with the standard pattern of nickel zinc ferrite (JCPDS 08-0234) [26]. Full Width at Half Maximum (FWHM) of the strongest reflection of the XRD pattern was utilized to estimate the average crystal size based on the Scherrer equation as following [27]:

$$D = k\lambda/\beta \cos\theta \quad (4)$$

Where k shows the shape function, 0.89, λ refers to the X-ray radiation wavelength, β refers to the FWHM at $2\theta=35.50^{\circ}$, and θ shows the diffraction angle. Based on the equation of Scherrer, the calculated value of D was 27.68 nm.

The $Ni_{0.2}Zn_{0.2}Fe_{2.6}O_4$ FE-SEM image in **Fig. 2A** indicates that the synthesized particles are nearly spherical in shape and homogenous in distribution with a diameter of less than 100 nm. **Fig. 2B** shows the distribution of the magnetic nanoparticles on the surface of the CA/CMC or embedding with the CA/CMC that confirms the successful synthesis of the CA/CMC/$Ni_{0.2}Zn_{0.2}Fe_{2.6}O_4$ magnetic bionanocomposite.

Fig. 3 indicates the FT-IR spectra of CA, CMC, $Ni_{0.2}Zn_{0.2}Fe_{2.6}O_4$, and CA/CMC/$Ni_{0.2}Zn_{0.2}Fe_{2.6}O_4$. The FT-IR spectra of CA and CMC respectively in **Figs. 3A** and **3B** show O-H stretching vibration at 3389 (CA) and 3436 (CMC) cm^{-1}, carboxylic groups asymmetrical stretching at 1622 (CA) and 1631 (CMC) cm^{-1}, carboxylic groups symmetrical stretching at 1423 (CA) and 1411 (CMC) cm^{-1} and C-O-C stretching at 1052 (CA) and 1061 (CMC) cm^{-1} [28,29]. The FT-IR spectrum of the $Ni_{0.2}Zn_{0.2}Fe_{2.6}O_4$ in **Fig. 3C** shows a broad absorption band with a value of 3424 cm^{-1} and less intensive band at 1633 cm^{-1} related to the O-H groups stretching vibration [30]. The bands at 2925 and 2853 cm^{-1} respectively correspond to the anti-symmetric and symmetric C-H vibrations of CTAB [31]. The band at 567 cm^{-1} relates to

the inherent metal stretching vibrations at the tetrahedral site (Fe-O), and the value of 478 cm^{-1} is related to the octahedral metal (M-O) stretching [30]. The comparison of the spectrum in **Fig. 3D** with other spectra expresses the successful synthesis of the CA/CMC/$Ni_{0.2}Zn_{0.2}Fe_{2.6}O_4$.

EDX was recorded to analyze the elements of the products (**Fig. 4**). **Fig. 4A** shows Ni, Zn, Fe, and O peaks that confirm the formation of the $Ni_{0.2}Zn_{0.2}Fe_{2.6}O_4$. The elemental analysis of the nanocomposite in **Fig. 4B** represents similar peaks available in **Fig. 4A** along with the new peaks for N and Ca because of combining the nanoparticles with CA and CMC. Sodium peak is not seen in the spectrum of the CA/CMC/$Ni_{0.2}Zn_{0.2}Fe_{2.6}O_4$, suggesting that sodium ions were released completely from the matrix of sodium alginate into the solution during the crosslinking reaction process of sodium alginate with calcium.

The CA/CMC/$Ni_{0.2}Zn_{0.2}Fe_{2.6}O_4$ weight loss curve recorded in the range of RT to 1000 $^{\circ}C$ is demonstrated in **Fig. 5A**. As it is seen, there are three different weight-loss steps in the TGA curve of the CA/CMC/$Ni_{0.2}Zn_{0.2}Fe_{2.6}O_4$. Obviously, the first step (around 190 $^{\circ}C$) with a weight loss of 8.77 % can be attributed to trapped and physisorbed water evaporation. The second step between around 190 and 550 $^{\circ}C$ is the largest weight loss with the amount of 35.08 % that could be due to the sorption and degradation of CA and CMC. The last step with 22.95 % weight loss at a temperature beyond 550 $^{\circ}C$ could be related to the further decomposition of CA and CMC and their conversion to CO_2 and H_2O. At the end of the process, the residue percentage is about 33.2 % that is principally assigned to the presence of the $Ni_{0.2}Zn_{0.2}Fe_{2.6}O_4$.

An important issue related to the magnetic bionanocomposite is that it should possess sufficient magnetic properties for its practical application. According to the magnetic hysteresis loops in **Fig. 5B**, the saturation magnetization value for $Ni_{0.2}Zn_{0.2}Fe_{2.6}O_4$ is about 45.87 emu/g that indicates superparamagnetic behavior of the synthesized product. It is obvious from **Fig. 5C**

that the process of the synthesis of the CA/CMC/$Ni_{0.2}Zn_{0.2}Fe_{2.6}O_4$ results in a decrease of saturation magnetization to the value of 14.14 emu/g. This decline is due to the combination of the magnetic nanoparticles with CA and CMC. Despite this difference, the ions-loaded CA/CMC/$Ni_{0.2}Zn_{0.2}Fe_{2.6}O_4$ could be easily separated by applying an external magnetic field from aqueous solution to avoid secondary pollution as indicated in **Fig. 5D.**

3.2. pH effect

pH of the solution as a key parameter of the adsorption process affects solution chemistry, metal speciation, adsorption capacity, the activity of adsorbent functional groups, and mechanism of adsorption. It is associated directly with H^+ competition with ions for the occupation of the surface active sites of the adsorbent. Adsorption efficiency values of Nd^{+3}, Tb^{+3}, and Dy^{+3} onto the CA/CMC/$Ni_{0.2}Zn_{0.2}Fe_{2.6}O_4$ as a pH function are demonstrated in **Fig. 6A**. Electrostatic interaction could have a key role on Nd^{+3}, Tb^{+3}, and Dy^{+3} adsorption onto the CA/CMC/$Ni_{0.2}Zn_{0.2}Fe_{2.6}O_4$ at different pH values. It can be interpreted that at lower pH values, the adsorption efficiency of the adsorbent is low and increase with increasing solution pH. At pH=1.5 that is highly acidic, the protonation of the adsorbent functional groups blocks the metal ions approach to the binding sites of the adsorbent. The metal ions and H^+ ions compete for the same binding sites of the adsorbent, leading to decrease in adsorption efficiency [32]. At pH=1.5, adsorption efficiency value is zero for all ions. When pH values are adjusted between 2.5 and 5.5, adsorption efficiency for Nd^{+3}, Tb^{+3}, and Dy^{+3} onto the CA/CMC/$Ni_{0.2}Zn_{0.2}Fe_{2.6}O_4$ increases with pH increase owing to the reduction in competition between H^+ ions and metal ions. The maximum adsorption efficiency for all metal ions occurs at pH=5.5. pH increase beyond 5.5 was not investigated to prohibit the precipitation of the ions in the form of hydroxide. Further experiments were carried out at pH=5.5 as optimum pH.

3.3. Contact time effect

It is essential to consider the adsorption rate in designing the batch experiments. The influence of contact time on Nd^{+3}, Tb^{+3}, and Dy^{+3} adsorption onto the CA/CMC/$Ni_{0.2}Zn_{0.2}Fe_{2.6}O_4$ bionanocomposite is shown in **Fig. 6B**. As can be observed, adsorption efficiency of the adsorbent increases rapidly during the first period and then increases slowly until reaching equilibrium state. The experimental outcomes indicate that Nd^{+3}, Tb^{+3}, and Dy^{+3} adsorption can be split into two definite parts: an extremely rapid initial adsorption occurs in the first 10 min, and then much slower adsorption is seen for higher contact time. In general, approximately 80 % of the metal ions contact quickly in the first 10 min because of the presence of largely accessible active sites of the adsorbent and then slowly increase owing to a gradual decrease in the active sites and weakness of the driving force and finally adsorption reaches equilibrium [33]. The contact time of 40 min was taken as an optimum time for adsorption of Nd^{+3}, Tb^{+3}, and Dy^{+3}.

3.4. Adsorbent dosage effect

The adsorbent dosage is considered as an important factor that affects the adsorption process and determines adsorbent capacity by the quantity of binding sites accessible for the adsorption of a specified initial concentration. **Fig. 6C** depicts the dependency of Nd^{+3}, Tb^{+3}, and Dy^{+3} adsorption efficiency to the adsorbent dosage. It expresses that Nd^{+3}, Tb^{+3}, and Dy^{+3} adsorption efficiency onto the adsorbent increase steeply (53.08–95.29, 51.4-94.43, and 59.04-96.1 %, respectively) by increasing adsorbent dosage in the range of 0.01 to 0.03 g. Although increasing the adsorbent dosage indicates an increase in number of binding sites available for ions adsorption, adsorption efficiency for all ions remains unchanged at a dosage higher than 0.04g since the adsorption reaches equilibrium. Therefore, the optimum dosage of 0.04 g in 50 mL solution (0.8g/L) was used for studying other adsorption parameters.

3.5. Initial concentration effect

Fig. 6D shows the adsorption efficiency values of the CA/CMC/$Ni_{0.2}Zn_{0.2}Fe_{2.6}O_4$ at different metal ions concentrations of 30 to 300 mg/L. It is demonstrated that the adsorption efficiency decreases by increasing the initial concentration because a given amount of the adsorbent has constant binding sites that are not enough at higher concentration to adsorb the ions, while calculating the capacity of the adsorbent showed that it respectively increased from 36.49 to 74.4, 36.31 to 103.23, and 36.68 to 118.17 mg/g for Nd^{+3}, Tb^{+3}, and Dy^{+3}. These results are due to a larger driving force at higher initial ion concentration that overcomes the whole mass transfer resistance available between the solid and liquid phases, causing more collisions between Nd^{+3}, Tb^{+3}, and Dy^{+3} and the active sites of the CA/CMC/$Ni_{0.2}Zn_{0.2}Fe_{2.6}O_4$ bionanocomposite that result in higher adsorption of the ions [34].

3.6. Adsorption kinetics and isotherms

Adsorption efficiency can be evaluated by adsorption kinetics as a key characteristic of adsorption process. Three kinetic methods namely pseudo-first-order (PFO), PSO, and intra-particle diffusion (IPD) were employed to fit the experimental data for the prediction of the kinetic parameters as following:

The PFO equation is written as follows [35]:

$$q_t = q_e\,(1 - \exp^{-K_1 t}) \qquad (5)$$

Where K_1 shows the PFO rate constant (1/min).

The PSO kinetic equation [36] is presented as follows:

$$q_t = K_2 q_e^2 t/1 + K_2 q_e t \qquad (6)$$

Where K_2 (g/mg min) shows PSO rate constant.

The initial adsorption rate (h) can be computed using the values of K_2 and q_e by the following equation:

$$h = K_2 q_e^2 \quad (7)$$

The IPD equation [37] is written as follows:

$$q_t = K_i t^{0.5} + C \quad (8)$$

Where K_i (1/min) refers to IPD rate constant, and C provides data about the boundary layer thickness: the greater value of C corresponds to the boundary layer diffusion influence.

For understanding the mechanism of the adsorption process, adsorption isotherms are applied. Langmuir and Freundlich isotherms were chosen as two important isotherm models in this study. Regarding Langmuir adsorption isotherm, monolayer adsorption occurs within the adsorbent at specific homogeneous sites. The nonlinear form of Langmuir isotherm is expressed using the following equation [38]:

$$q_e = \frac{b\, qm\, Ce}{(1+bCe)} \quad (9)$$

Where q_e and q_m (mg/g) respectively show the equilibrium capacity of adsorption and the maximum adsorption capacity. C_e (mg/L) is ion equilibrium concentration, and b (L/mg) shows the constant of Langmuir model.

The main characteristic of Langmuir model is indicated by 'R_L', which is a dimensionless constant that is generally known as separation factor or equilibrium parameter. It is indicated by the bellowing equation:

$$R_L = \frac{1}{1+bC_i} \quad (10)$$

Where C_i (mg/L) shows the greatest initial metal concentration.

Freundlich isotherm is performed to explain heterogeneous systems. The nonlinear form of Freundlich isotherm is presented as follows [39]:

$$q_e = K C_e^{1/n} \quad (11)$$

Where K ($mg^{1-1/n}$ $L^{1/n}/g$) refers to the constant of Freundlich isotherm, and n shows adsorption intensity. A value of $n > 1$ expresses that adsorption is desirable.

Fitting the experimental data with the kinetic and isotherm models was optimized by error analysis. In this study, Chi-square (χ^2) was used to compare the validity of each model by the following equation:

$$\chi^2 = \sum_{i=1}^{n} \frac{(q_{e,exp} - q_{e,cal})^2}{q_{e,cal}} \quad (12)$$

Where $q_{e,exp}$ and $q_{e,cal}$ respectively refer to the experimental and computed adsorbent capacities, and n shows data point numbers.

Table 1 indicates essential parameters computed from the kinetic models. The theoretical values of q_e obtained from PFO kinetic model in Nd^{+3}, Tb^{+3}, and Dy^{+3} adsorption are not in agreement with the experimental values, while the experimental values of q_e ($q_{e,exp}$) are close to theoretical q_e ($q_{e,cal}$) values calculated by PSO model. The coefficient of determination values obtained by fitting the data with PFO model are lower than those of PSO model. Consequently, PSO model can be chosen to fit the data more efficiently compared to PFO model. According to IPD model, involving IPD in adsorption process creates a linear plot of uptake, q_t versus $t^{0.5}$. Furthermore, the rate controlling step is shown by IPD model if the lines pass through the origin. The values of R^2 show that IPD model is not appropriate for explaining the adsorption kinetic. The values of R^2 and error analyses obtained by PSO kinetic model are respectively the highest and lowest values. Therefore, Nd^{+3}, Tb^{+3}, and Dy^{+3} adsorption onto the CA/CMC/$Ni_{0.2}Zn_{0.2}Fe_{2.6}O_4$ are well described by PSO model. The results express that the rate-limiting step in Nd^{+3}, Tb^{+3}, and Dy^{+3} adsorption is chemisorption that involves valence forces by exchanging or sharing electrons between the adsorbent and the ions. The K_2 value from the PSO

model for Dy^{+3} is greater than the values obtained for Nd^{+3} and Tb^{+3} ions, suggesting that Dy^{+3} adsorption onto the adsorbent is faster than those of Nd^{+3} and Tb^{+3} ions. From the results of isotherm fitting shown in **Table 2**, Tb^{+3} and Dy^{+3} adsorption data for the CA/CMC/$Ni_{0.2}Zn_{0.2}Fe_{2.6}O_4$ were fitted well with Freundlich isotherm model with the R^2 values of 0.9905 and 0.9751, respectively, suggesting the adsorption of the ions on heterogeneous sites. In the case of Nd^{+3}, the data of adsorption were efficiently fitted with Langmuir isotherm with the R^2 value of 0.9703, suggesting that the Langmuir surface adsorption mechanism controls the adsorption of Nd^{+3} onto the CA/CMC/$Ni_{0.2}Zn_{0.2}Fe_{2.6}O_4$. Therefore, it can be mentioned that the number of adsorption sites of the adsorbent is limited that leads to the monolayer adsorption of Nd^{+3}, and no further adsorption occurs when covering the active sites with the ions takes place. R_L exhibits favorable isotherm if $0 < R_L < 1$, unfavorable if $R_L > 1$, irreversible if $R_L = 0$ or linear if $R_L = 1$ [40]. R_L value in **Table 2** is between 0 and 1 for Nd^{+3}, Tb^{+3}, and Dy^{+3} adsorption onto the CA/CMC/$Ni_{0.2}Zn_{0.2}Fe_{2.6}O_4$, indicating that the adsorption process is favorable. The values of n for adsorption of the ions are higher than 1, representing a favorable adsorption condition. A comparison of the adsorption capacity of different adsorbents is represented in **Table 3**.

3.7. Ionic strength effect

It has been confirmed that salts presence in the solution can affect adsorption efficiency. The adsorption efficiency of Nd^{+3}, Tb^{+3}, and Dy^{+3} was studied in the existence of $NaNO_3$ in the range of 0.02 to 0.1 M at the constant concentration of the ions (30 mg/L). The obtained results are indicated in **Fig. 7A**. The adsorption efficiency of the adsorbent decreases for Nd^{+3}, Tb^{+3}, and Dy^{+3} from 97.75 to 85.7, 96.83 to 84.73, and 97.85 to 93.5 %, respectively, that shows the ionic strength slightly affects on the adsorption of Dy^{+3} in comparison with the decrease obtained for

Nd^{+3} and Tb^{+3}. The decrease in the adsorption efficiency could be associated with Na^{+} ions competition with the metal ions for the CA/CMC/$Ni_{0.2}Zn_{0.2}Fe_{2.6}O_4$ active adsorption sites [64]. Enhancing Na^{+} ion concentration may also lead to a reduction in the activity coefficient of the metal ions that cause the limitation of the ions transfer to the adsorbent surface [65].

3.8. Temperature effect

The temperature influence on the adsorption efficiency of Nd^{+3}, Tb^{+3}, and Dy^{+3} onto the CA/CMC/$Ni_{0.2}Zn_{0.2}Fe_{2.6}O_4$ bionanocomposite was studied by performing the experiments at various temperatures (25, 35, and 45 $^{\circ}$C), and the results are demonstrated in **Table 4**. As can be observed, the adsorption efficiency increases for all metal ions with temperature increase that may be owing to the increase in metal ions mobility and their tendency to be adsorbed onto the adsorbent surface, and due to higher activity of the binding sites with an increase in temperature as well.

3.9. Thermodynamic parameters evaluation

The ΔH° and ΔS° thermodynamic parameters were computed as follows [66]:

$$\text{Ln } K_d = \frac{\Delta S^{\circ}}{R} - \frac{\Delta H^{\circ}}{RT} \quad (13)$$

Where R shows the gas constant (8.314 J/mol K), and T refers to the temperature (K). The intercept and slope of the curves of Ln K_d versus 1/T are used to calculate the values of ΔS° and ΔH°, respectively (**Fig. 7B**).

K_d demonstrates the distribution coefficient that was obtained by the following equation [67]:

$$K_d = \frac{q_e}{C_e} \quad (14)$$

The ΔG° quantities were also computed at different temperatures utilizing the bellowing equation [68]:

$$\Delta G^{\circ} = - RT \text{ Ln } K_d \quad (15)$$

The obtained thermodynamic parameters at different temperatures in **Table 4** indicate that Nd^{+3}, Tb^{+3}, and Dy^{+3} adsorption onto the CA/CMC/$Ni_{0.2}Zn_{0.2}Fe_{2.6}O_4$ is naturally feasible and spontaneous due the negative quantities of Gibbs free energy changes. In addition, by increasing temperature from 25 $^{\circ}$C to 35 and 45 $^{\circ}$C, the value of Gibbs free energy change for Nd^{+3}, Tb^{+3}, and Dy^{+3} adsorption onto the adsorbent becomes more negative, indicating more feasibility of the adsorption of the metal ions onto the adsorbent at higher temperature [67]. The ΔH° positive values suggest the endothermic adsorption process of Nd^{+3}, Tb^{+3}, and Dy^{+3} onto the adsorbent [66]. Furthermore, the ΔS° positive values indicate that the randomness and disorder at the solid-solution interface increases during the adsorption of the ions [68].

3.10. Reusability studies

The results of the ions adsorption efficiency of the adsorbent regarding the cycle number by 0.04 g of the adsorbent are displayed in **Fig. 7C**. As can be seen, the highest adsorption efficiency of Nd^{+3}, Tb^{+3}, and Dy^{+3} adsorption is related to the first cycle because the number of fresh active sites existing on the adsorbent surface for Nd^{+3}, Tb^{+3}, and Dy^{+3} adsorption is abundant; therefore, adsorption occurs through the stronger bonds. It is seen that the first cycle respectively results in adsorption efficiencies of 96.72, 96.32, and 97.12 % for Nd^{+3}, Tb^{+3}, and Dy^{+3} by the CA/CMC/$Ni_{0.2}Zn_{0.2}Fe_{2.6}O_4$. The adsorption efficiency for the metal ions is found to be decreased during the four adsorption-desorption cycles; nevertheless, the reduction is not so significant. The obtained results at the end of the fourth cycle signify that the adsorption efficiency of the CA/CMC/$Ni_{0.2}Zn_{0.2}Fe_{2.6}O_4$ remains more than 95, 94, and 95 % for Nd^{+3}, Tb^{+3}, and Dy^{+3}, respectively, and the slight decrease in adsorption efficiency could be related to the fact that Nd^{+3}, Tb^{+3}, and Dy^{+3} are not released from adsorption sites during the cycles, leading to the

inactivation of a portion of the surface sites. The obtained results suggest the CA/CMC/$Ni_{0.2}Zn_{0.2}Fe_{2.6}O_4$ as a recyclable adsorbent for Nd^{+3}, Tb^{+3}, and Dy^{+3} adsorption.

3.11. Competitive adsorption

To evaluate competitive adsorption of Nd^{+3}, Tb^{+3}, and Dy^{+3} in the ternary system of 30 mg/L (1:1:1), 0.04 g of the CA/CMC/$Ni_{0.2}Zn_{0.2}Fe_{2.6}O_4$ (the same as a single system) was used. According to the value of q_{mix}/q_0, three kinds of influences including antagonism, synergism, and non-interaction can occur in a multicomponent system as following:

- Antagonism ($q_{mix}/q_0 < 1$): the influence of component mixture in solution is lower than its influence in single mode.
- Synergism ($q_{mix}/q_0 > 1$): the influence of component mixture in solution is higher than its influence in single mode.
- Non-interaction ($q_{mix}/q_0 = 1$): the influence of the component mixture in solution is neither less nor more compared with its influence in single mode.

Where q_{mix} and q_0 are the adsorption capacities of each ion in the mixture and single systems, respectively.

The value of q_{mix}/q_0 for each ion was respectively calculated to be 0.27, 0.5, and 0.52 for Nd^{+3}, Tb^{+3} and Dy^{+3}. The obtained results state that the q_{mix}/q_0 value for all ions is less than 1 in a ternary mixture; therefore, the existence of each ion shows an antagonism influence on the adsorption of other ions in the process. The adsorption efficiency of the adsorbent for Nd^{+3}, Tb^{+3}, and Dy^{+3} decreased to 28.25, 48.62, and 50.58 %, respectively. EDX spectrum was also recorded after the ions adsorption process, and the result is illustrated in **Fig. 7D**. The existence of Nd^{+3}, Tb^{+3}, and Dy^{+3} in the spectrum strongly confirms the successful adsorption of these ions from a ternary mixture by the CA/CMC/$Ni_{0.2}Zn_{0.2}Fe_{2.6}O_4$.

4. Conclusion

The goal of this research work was to synthesize the CA/CMC/$Ni_{0.2}Zn_{0.2}Fe_{2.6}O_4$ as a novel magnetic bionanocomposite adsorbent for adsorption of Nd^{+3}, Tb^{+3}, and Dy^{+3} from aqueous media. The adsorbent was characterized by FE-SEM, EDX, XRD, FT-IR, EDX, and VSM techniques, and the influence of different factors such as pH, contact time, adsorbent dosage, initial concentration, ionic strength, and temperature was considered by batch adsorption tests. The maximum adsorption capacity of the CA/CMC/$Ni_{0.2}Zn_{0.2}Fe_{2.6}O_4$ for Nd^{+3} acquired by Langmuir isotherm model was 73.37 mg/g at pH = 5.5, while Freundlich model fitted the Tb^{+3} and Dy^{+3} adsorption data at the same conditions. Kinetic studies indicated that PSO with the highest R^2 and lowest error can describe the adsorption mechanism of the metal ions. The results obtained from affecting $NaNO_3$ as ionic strength showed a slight reduction in the values of adsorption efficiency. The values of the parameters of thermodynamic (ΔG°, ΔS°, and ΔH°) demonstrated that the metal ions adsorption was endothermic and spontaneous in nature. 0.2 M HNO_3 easily desorbed the ions, and the adsorbent was utilized four times with the adsorption efficiency values of more than 95, 94, and 95 % for Nd^{+3}, Tb^{+3}, and Dy^{+3}, respectively, at the end of the fourth cycle. The results of this study showed the CA/CMC/$Ni_{0.2}Zn_{0.2}Fe_{2.6}O_4$ as a promising novel adsorbent for Nd^{+3}, Tb^{+3}, and Dy^{+3} adsorption.

Acknowledgments

This work has been supported by the Spanish Ministry of Economy and Competitiveness (Ref. CTM2017-83581-R). Hamedreza Javadian acknowledges the financial support received (Ref. BES-2015-072506).

References

[1] J. Ponou, L.P. Wang, S. Matsuo, G. Dodbiba, T. Fujita, Recovery of dysprosium ions by biosorption-desorption onto organic plants wastes, Int. J. Soc. Mater. 20 (2014) 141-146.

[2] K. Vidal, L. Ortega-San-Martin, A. Larranaga, R.I. Merino, A. Orera, M.I. Arriortua, Effects of synthesis conditions on the structural, stability and ion conducting properties of $Li_{0.30}(La_{0.50}Ln_{0.50})_{0.567}TiO_3$ (Ln = La, Pr, Nd) solid electrolytes for rechargeable lithium batteries, Ceram. Int. 40 (2014) 8761−8768.

[3] X.Xu, J. Zou, X.R Zhao, X.Y Jiang, F.P Jiao, J.G. Yu, Q. Liu, J. Teng, Facile assembly of three-dimensional cylindrical egg white embedded graphene oxide composite with good reusability for aqueous adsorption of rare earth elements, Colloids Surf., A. 570 (2019) 127-140.

[4] K. Binnemans, P. Tom Jones, B. Blanpain, T. Van Gerven, Y. Yang, A. Walton, M. Buchert, Recycling of rare earths: a critical review, J. Clean. Prod. 51 (2013) 1-22.

[5] A.H. King, R.G. Eggert, K.A. Gschneidner Jr, The rare earths as critical materials, Handbook on the Physics and Chemistry of Rare Earths, 50 (2016) 19-46.

[6], Z.V.P. Murthy, A. Choudhary, Separation and estimation of nanofiltration membrane transport parameters for cerium and neodymium. Rare Met. 31 (2012) 500−506.

[7] S.J. Nejad, H. Abolghasemi, M.A. Moosavian, M.G. Maragheh, Fractional factorial design for the optimization of supercritical carbon dioxide extraction of La^{3+}, Ce^{3+} and Sm^{3+} ions from a solid matrix using Bis(2,4,4-Trimethylpentyl)Dithiophosphinic acid plus tributylphosphate, Chem. Eng. Res. Des. 89 (2011) 827−835.

[8] R. Kala, T.P. Rao, Ion imprinted polymer particles for separation of Yttrium from selected lanthanides. J. Sep. Sci. 29 (2006) 1281−1287.

[9] X. Wang, L. Chen, L. Wang, Q. Fan, D. Pan, J. Li, F. Chi, Y. Xie, S. Yu, C. Xiao, F. Luo, J. Wang, X. Wang, C. Chen, W. Wu, W. Shi, S. Wang, X. Wang, Synthesis of novel nanomaterials and their application in efficient removal of radionuclides, Sci China Chem 62 (2019) 933–967.

[10] X. Liu, R. Ma, X. Wang, Y. Ma, Y. Yang, L. Zhuang, S. Zhang, R. Jehan, J. Chen, X. Wang, Graphene oxide-based materials for efficient removal of heavy metal ions from aqueous solution: A review, Environ Pollut 252 (2019) 62-73.

[11] D.B. Wu, J. Zhao, L. Zhang, Q.S. Wu, Y.H. Yang, Lanthanum adsorption using iron oxide loaded calcium alginate beads. Hydrometallurgy 101 (2010) 76−83.

[12] D.B. Wu, L. Zhang, L. Wang, B.H. Zhu, L.Y. Fan, Adsorption of lanthanum by magnetic alginate-chitosan gel beads. J. Chem. Technol. Biotechnol. 86 (2011) 345−352.

[13] L. Zhang, D.B. Wu, B.H. Zhu, Y.H. Yang, L. Wang, Adsorption and selective separation of neodymium with magnetic alginate microcapsules containing the extractant 2-ethylhexyl phosphonic acid mono-2-ethylhexyl ester. J. Chem. Eng. Data 56 (2011) 2280−2289.

[14] N.S. Awwad, H.M.H. Gad, M.I. Ahmad, H.F. Aly, Sorption of lanthanum and erbium from aqueous solution by activated carbon prepared from rice husk. Colloids Surf., B. 81 (2010) 593−599.

[15] S.M.A. Koochaki-Mohammadpour, M. Torab-Mostaedi, A. Talebizadeh-Rafsanjani, F. Naderi-Behdani, Adsorption isotherm, kinetic, thermodynamic, and desorption studies of lanthanum and dysprosium on oxidized multiwalled carbon nanotubes. J. Dispersion Sci. Technol. 35 (2014) 244−254.

[16] T.A. Saleh, Nanocomposite of carbon nanotubes/silica nanoparticles and their use for adsorption of Pb (II): from surface properties to sorption mechanism, Desalination and Water Treatment 57 (23), (2016) 10730-10744.

[17] F. Granados-Correa, J. Vilchis-Granados, M. Jimenez-Reyes, L.A. Quiroz-Granados, Adsorption behaviour of La(III) and Eu(III) ions from aqueous solutions by hydroxyapatite: Kinetic, isotherm, and thermodynamic studies. J. Chem. 2013 (2013) 1−9.

[18] D.B. Wu, C.M. Zhu, Y.G. Chen, B.H. Zhu, Y.H. Yang, Q.G. Wang, W.M. Ye, Preparation, characterization and adsorptive study of rare earth ions using magnetic GMZ bentonite. Appl. Clay Sci. 62−63 (2012) 87−93.

[19] G.S. Hong, L.D. Shen, M. Wang, Y. Yang, X.F. Wang, M.F. Zhu, B.S. Hsiao, Nanofibrous polydopamine complex membranes for adsorption of lanthanum (III) ions. Chem. Eng. J. 244 (2014) 307−316.

[20] M.A. Maheswari, M.S. Subramanian, Extraction chromatographic method for the separation of actinides and lanthanides using EDHBA grafted AXAD-16 polymer. Talanta. 65 (2005) 735−742.

[21] W.M. Algothmi, N. Murthy Bandaru, Y. Yu, J.G. Shapter, A.V. Ellis, Alginate-graphene oxide hybrid gel beads: An efficient copper adsorbent material, J. Colloid Interface Sci. 397 (2013) 32-38.

[22] H. Hecht, S. Srebnik, Structural characterization of sodium alginate and calcium alginate, Biomacromolecules. 17 (2016) 2160-2167.

[23] M. Rinaudo, Chitin and chitosan: properties and applications, Prog. Polym. Sci. 31 (2006) 603–632.

[24] S. Zinadini, A.A. Zinatizadeh, M. Rahimi, V. Vatanpour, H. Zangeneh, M. Beygzadeh, Novel high flux antifouling nanofiltration membranes for dye removal containing carboxymethyl chitosan coated Fe_3O_4 nanoparticles, Desalination 349 (2014) 145–154.

[25] F.C. Wang, J.M. Zhao, H.C. Zhou, W. Li, N. Sui, H. Liu, O-carboxymethyl chitosan entrapped by silica: preparation and adsorption behaviour toward neodymium(III) ions, J. Chem. Technol. Biot. 88 (2013) 317–325.

[26] D. Ni, Z. Lin, P. Xiaoling, W. Xinqing, G. Hongliang, Preparation and characterization of nickel-zinc ferrites by a solvothermal method, Rare Metal Mat Eng. 44 (9) (2015) 2126-2131.

[27] M. Sundararajan, P. Sakthivel, A. Christina Fernandez, Structural, optical and electrical properties of ZnO-ZnS nanocomposites prepared by simple hydrothermal method, J. Alloy Compd. 768 (2018) 553-562.

[28] C. Larosa, M. Salerno, J. Silva de Lima, R. Merijs Meri, M. Fernandes da Silva, L. Bezerra de Carvalho, A. Converti, Characterisation of bare and tannase-loaded calcium alginate beads by microscopic, thermogravimetric, FTIR and XRD analyses, Int. J. Biol. Macromol. 115 (2018) 900–906.

[29] T.A. Saleh, Isotherm, kinetic, and thermodynamic studies on Hg (II) adsorption from aqueous solution by silica-multiwall carbon nanotubes, Environmental Science and Pollution Research 22 (21), (2015) 16721-16731.

[30] G. Fadillah, T.A. Saleh, S. Wahyuningsih, ENK Putri, S. Febrianastuti, Electrochemical removal of methylene blue using alginate-modified graphene adsorbents, Chemical Engineering Journal 378 (2019) 122140.

[31] S.A. Elfeky, S. Ebrahim Mahmoud, A. Fahmy Youssef, Applications of CTAB modified magnetic nanoparticles for removal of chromium (VI) from contaminated water, J. Adv. Res. 8(4) (2017) 435–443.

[32] H. Abdolmohammad-Zadeh, Z. Ayazi, Z. Naghdi, Nickel oxide/chitosan nano-composite as a magnetic adsorbent for preconcentration of Zn(II) ions, J. Magn. Magn. Mater. 488 (2019) 165311

[33] X. Huang, D. Wei, X. Zhang, D. Fan, X. Sun, B. Du, Q. Wei, Synthesis of amino-functionalized magnetic aerobic granular sludge-biochar for Pb(II) removal: Adsorption performance and mechanism studies, Sci. Total Environ. 685 (2019) 681–689.

[34] H. Lu, Y. Li, Y. Wang, X. Li, Preparation of $CoFe_2O_4$@vacancy@mSiO_2 core-shell composites for removal of organic pollutant in aqueous solution, J. Saudi Chem. Soc. 23 (2019) 536-545.

[35] N.H. Kera, M. Bhaumik, K. Pillay, S. Sinha Ray, A. Maity, Selective removal of toxic Cr(VI) from aqueous solution by adsorption combined with reduction at a magnetic nanocomposite surface, J. Colloid Interface Sci. 503 (2017) 214-228.

[36] H. Javadian, F. Ghorbani, H. Tayebi, S.M. Hosseini Asl, Study of the adsorption of Cd (II) from aqueous solution using zeolite-based geopolymer, synthesized from coal fly ash; kinetic, isotherm and thermodynamic studies, Arab. J. Chem. 8 (2015) 837-849.

[37] H. Javadian, F. Zamani Sorkhrodi, B. Babzadeh Koutenaei, Experimental investigation on enhancing aqueous cadmium removal via nanostructure composite of modified hexagonal type mesoporous silica with polyaniline/polypyrrole nanoparticles, J. Ind. Eng. Chem. 20 (2014) 3678-3688.

[38] M.A. Espinade Franco, C. Bonfantede Carvalho, M. Marques Bonetto, R. de Pelegrini Soares, L. Amaral Féris, Diclofenac removal from water by adsorption using activated carbon in batch mode and fixed-bed column: Isotherms, thermodynamic study and breakthrough curves modeling, J. Clean. Prod. 181 (2018) 145-154.

[39] A. Cristiana Fröhlich, E. Luiz Foletto, G. Luiz Dotto, Preparation and characterization of $NiFe_2O_4$/activated carbon composite as potential magnetic adsorbent for removal of ibuprofen and ketoprofen pharmaceuticals from aqueous solutions, J. Clean. Prod. 229 (2019) 828-837.

[40] H. Javadian, Adsorption performance of suitable nanostructured novel composite adsorbent of poly(N-methylaniline) for removal of heavy metal from aqueous solutions, J. Ind. Eng. Chem. 20 (2014) 4344-4352.

[41] E. Liu, X. Zheng, X. Xu, F. Zhang, E. Liu, Y. Wang, C. Li, Y. Yan, Preparation of diethylenetriamine-modified magnetic chitosan nanoparticles for adsorption of rare-earth metal ions, New J. Chem. 41 (2017) 7739-7750.

[42] J. Roosen, K. Binnemans, Adsorption and chromatographic separation of rare earths with EDTA- and DTPAfunctionalized chitosan biopolymers. J Mater Chem A. 2 (2014) 1530–1540.

[43] I.V. Melnyk, V.P. Goncharyk, L.I. Kozhara, G.R. Yurchenko, A.K. Matkovsky, Y.L. Zub, B. Alonso, Sorption properties of porous spray-dried microspheres functionalized by phosphonic acid groups, Microporous Mesoporous Mater. 153 (2012) 171–177.

[44] T. Kegl, I. Ban, A. Lobnik, A. Košak, Synthesis and characterization of novel γ-Fe_2O_3-$NH_4OH@SiO_2$(APTMS) nanoparticles for dysprosium adsorption, J. Hazard. Mater. 378 (2019) 120764.

[45] A. Negrea, A. Gabor, C.M. Davidescu, M. Ciopec, P. Negrea, N. Duteanu, A. Barbulescu, Rare earth elements removal from water using natural polymers, Sci Rep. 8 (2018) 316.

[46] Y.R. Lee, K. Yu, S. Ravi, W.S. Ahn, Selective adsorption of rare earth elements over functionalized Cr-MIL-101. Appl Mater Interfaces. 10 (2018) 23918-23927.

[47] X-H. Qi, K-Z Du, M-L Feng, Y-J Gao, X-Y. Huang, M.G. Kanatzidis, Layered $A_2Sn_3S_7 \cdot 1.25H_2O$ (*A* = organic cation) as efficient ion-exchanger for rare earth element recovery, J. Am. Chem. Soc. 2017, 139, 12, 4314-4317.

[48] S.M.A. Koochaki-Mohammadpour, M. Torab-Mostaedi, A. Talebizadeh-Rafsanjani, F. Naderi-Behdani, Adsorption isotherm, kinetic, thermodynamic, and desorption studies of lanthanum and dysprosium on oxidized multiwalled carbon nanotubes. J Dispers Sci Technol 35 (2014) 244–254.

[49] M.M. Yusoff, N.R. Nik Mostapa, Md. Shaheen Sarkar, T.K. Biswas, Md. Lutfor Rahman, S.E. Arshad, M.S. Sarjadi, A.D. Kulkarni, Synthesis of ion imprinted polymers for selective recognition and separation of rare earth metals, J. Rare Earth 35 (2017) 177-186.

[50] H.A. Madbouly, N.E. El-Hefny, Y.A. El-Nadi, Adsorption and separation of terbium(III) and gadolinium(III) from aqueous nitrate medium using solid extractant, Sep Sci Technol. (2019) 1-13.

[51] S. Tong, S. Zhao, W. Zhou, R. Li, Q. Jia, Modification of multi-walled carbon nanotubes with tannic acid for the adsorption of La, Tb and Lu ions, Microchim Acta 174 (2011) 257–264.

[52] D. Baybaş, U. Ulusoy, Polyacrylamide–clinoptilolite/Y-zeolite composites: Characterization and adsorptive features for terbium, J Hazard Mater 187(1) (2011) 241–249.

[53] R. Akkaya, Synthesis and characterization of a new low-cost composite for the adsorption of rare earth ions from aqueous solutions, Chem Eng J 200 (2012) 186–191.

[54] R. Akkaya, Terbium adsorption onto polyhydroxyethylmethacrylate–hydroxyapatite composite and its modified composition by phytic acid, Desalin Water Treat 52 (2014) 1440-1447.

[55] F.A. Alakhras, K.A. Dari, M.S. Mubarak, Synthesis and chelating properties of some Poly (Amidoxime-hydroxamic Acid) resins toward some trivalent lanthanide metal ions, J Appl Polym Sci 97(2) (2005) 691–696.

[56] M.A. Attia, S.I. Moussa, R.R. Sheha, H.H. Someda, E.A. Saad, Hydroxyapatite/$NiFe_2O_4$ superparamagnetic composite: Facile synthesis and adsorption of rare elements, Appl. Radiat. Isot. 145 (2019) 85-94.

[57] N.S. Reddy, K.M. Rao, S.V. Krishna, C.S. Ha, Synthesis of 1–acryloyl–3–phenyl thiourea based pH sensitive hydrogels for removal of samarium and terbium. Macromol. Res. 24 (2016) 494–501.

[58] M.R. Awual, N.H. Alharthi, Y. Okamoto, M.R. Karim, M.E. Halim, M.M. Hasan, M.M. Rahman, M.M. Islam, M.A. Khaleque, M.C. Sheikh, Ligand field effect for Dysprosium(III) and Lutetium(III) adsorption and EXAFS coordination with novel composite nanomaterials, Chem. Eng. J. 320 (2017) 427-435.

[59] R.M. Ashour, R. El-Sayed, A.F. Abdel-Magied, A.A. Abdel-Khalek, M.M. Ali, K. Forsberg, A. Uheida, M. Muhammed, J. Dutta, Selective separation of rare earth ions from aqueous solution using functionalized magnetite nanoparticles: kinetic and thermodynamic studies, Chem. Eng. J. 327 (2017) 286–296.

[60] H. Aghayan, A. Mahjoub, A. Khanchi, Samarium and dysprosium removal using 11-molybdo-vanadophosphoric acid supported on Zr modified mesoporous silica SBA-15, Chem. Eng. J. 225 (2013) 509–519.

[61] T. Kaneko, F. Nagata, S. Kugimiya, K. Katob, Optimization of carboxyl-functionalized mesoporous silica for the selective adsorption of dysprosium, J Environmen Chem Eng 6 (2018) 5990-5998.

[62] X. Zheng, Y. Zhang, T. Bian, Y. Zhang, Z. Li, J. Pan, Oxidized carbon materials cooperative construct ionic imprinted cellulose nanocrystals films for efficient adsorption of Dy(III), Chem Eng J 381 (2020) 122669.

[63] X. Zheng, E. Liu, F. Zhang, Y. Yan, J. Pan, Efficient adsorption and separation of dysprosium from NdFeB magnets in an acidic system by ion imprinted mesoporous silica sealed in a dialysis bag, Green Chem. 18 (2016) 5031–5040.

[64] İ. Kara, D. Yilmazer, S. Tunali Akar, Metakaolin based geopolymer as an effective adsorbent for adsorption of zinc(II) and nickel(II) ions from aqueous solutions, Appl. Clay Sci. 139 (2017) 54–63.

[65] D. Alipour, A.R. Keshtkar, M.A. Moosavian, Adsorption of thorium (IV) from simulated radioactive solutions using a novel electrospun PVA/TiO_2/ZnO nanofiber adsorbent functionalized with mercapto groups: Study in single and multi-component systems, Appl. Surf. Sci. 366 (2016) 19–29.

[66] M. Rajabi, K. Mahanpoor, O. Moradi, Preparation of PMMA/GO and PMMA/GO-Fe_3O_4 nanocomposites for malachite green dye adsorption: Kinetic and thermodynamic studies Compos Part B Eng. 167 (2019) 544-555.

[67] H. Javadian, P. Vahedian, M. Toosi, Adsorption characteristics of Ni(II) from aqueous solution and industrial wastewater onto Polyaniline/HMS nanocomposite powder, Appl. Surf. Sci. 284 (2013) 13-22.

[68] N. Subedi, A. Lähde, E. Abu-Danso, J. Iqbal, A. Bhatnagar, A comparative study of magnetic chitosan (Chi@Fe_3O_4) and graphene oxide modified magnetic chitosan (Chi@Fe_3O_4GO) nanocomposites for efficient removal of Cr(VI) from water, Int. J. Biol. Macromol. 137 (2019) 948–959.

Credit author statement

Hamedreza Javadian: Investigation, Acquisition of data, Analysis and/or interpretation of data, Drafting the manuscript and Revising the manuscript. **Montsserat Ruiz**: Acquisition of data and Supervision. **Tawfik A. Saleh**: Revising the manuscript. **Ana Maria Sastre**: Conceptualization and supervision.

Conflict of Interest

There is not conflict of interest

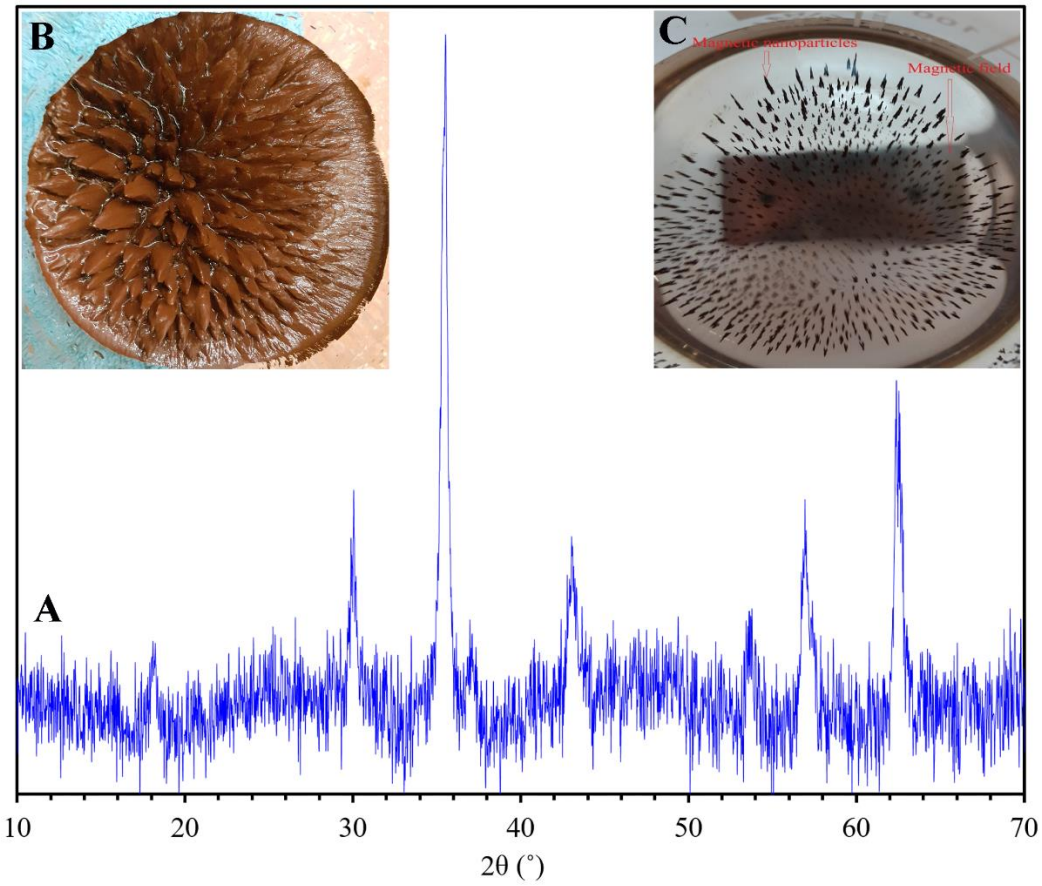

Fig. 1. (A) XRD pattern of $Ni_{0.2}Zn_{0.2}Fe_{2.6}O_4$ nanopartciles; Photo of $Ni_{0.2}Zn_{0.2}Fe_{2.6}O_4$ nanoparticles (B) before drying and (C) in the solution under magnetic field after drying.

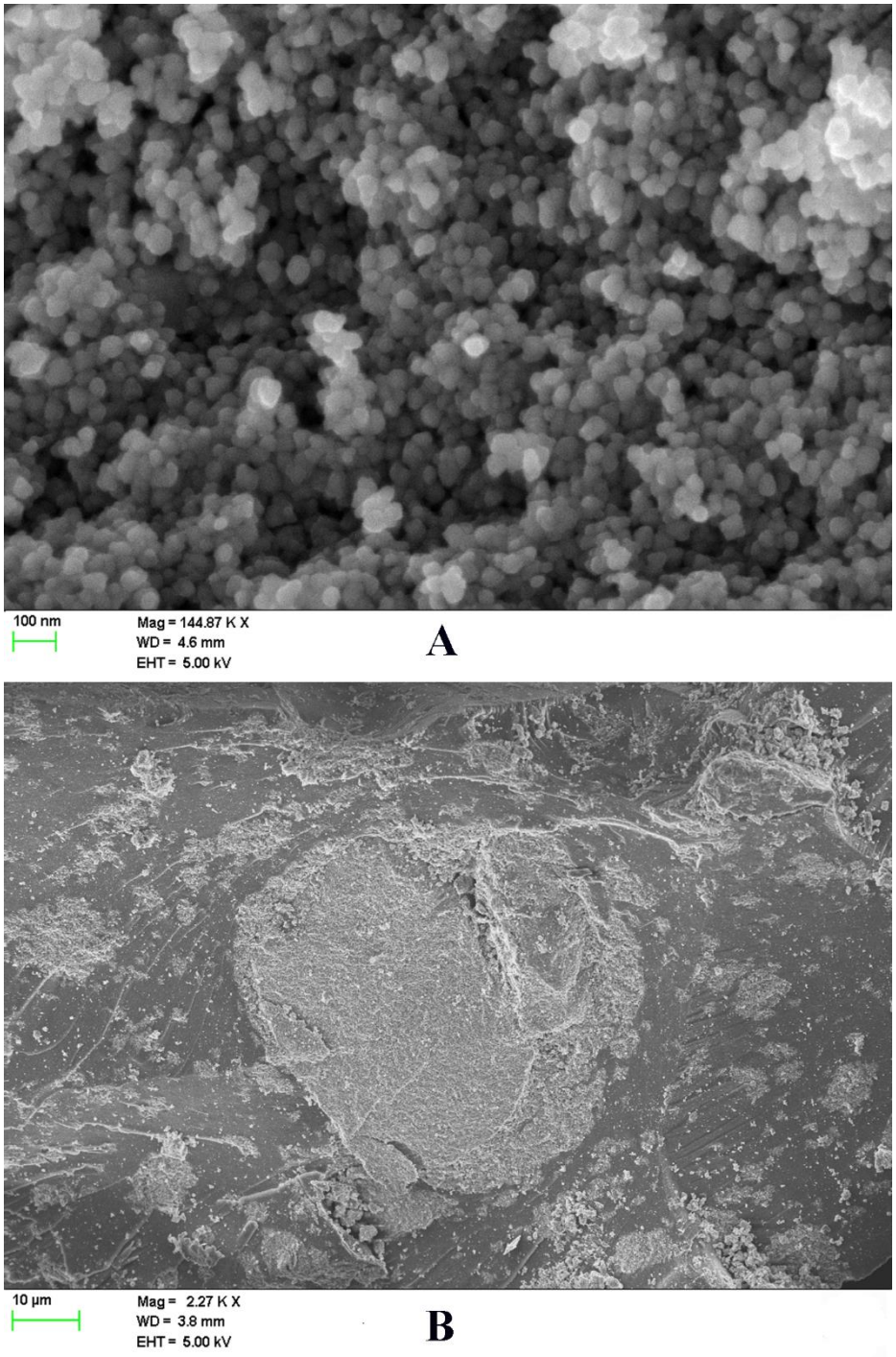

Fig. 2. FE-SEM images of (A) $Ni_{0.2}Zn_{0.2}Fe_{2.6}O_4$ and (B) CA/CMC/$Ni_{0.2}Zn_{0.2}Fe_{2.6}O_4$.

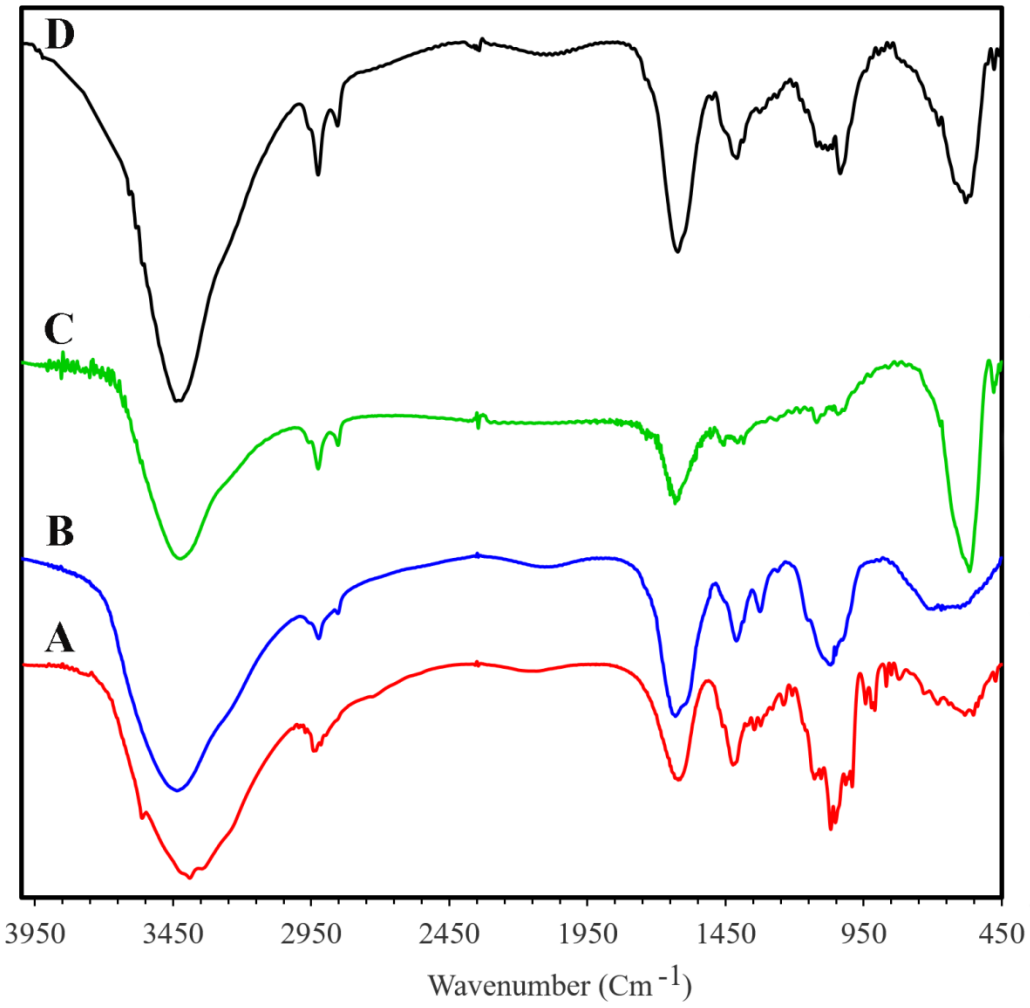

Fig. 3. FT-IR spectra of (A) CA, (B) CMC, (C) $Ni_{0.2}Zn_{0.2}Fe_{2.6}O_4$, and (D) CA/CMC/$Ni_{0.2}Zn_{0.2}Fe_{2.6}O_4$.

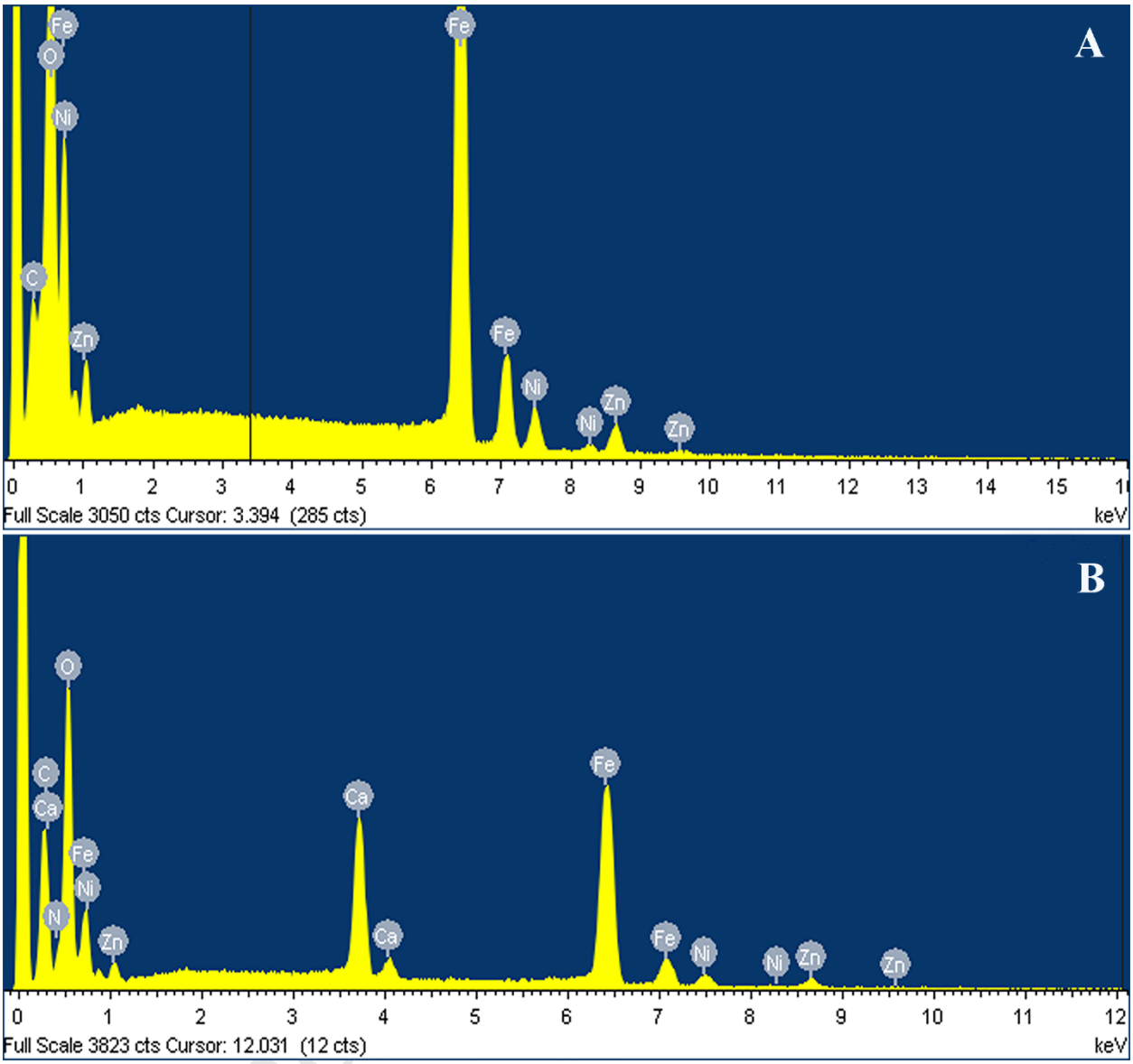

Fig. 4. EDX spectra of (A) $Ni_{0.2}Zn_{0.2}Fe_{2.6}O_4$ and (B) CA/CMC/$Ni_{0.2}Zn_{0.2}Fe_{2.6}O_4$.

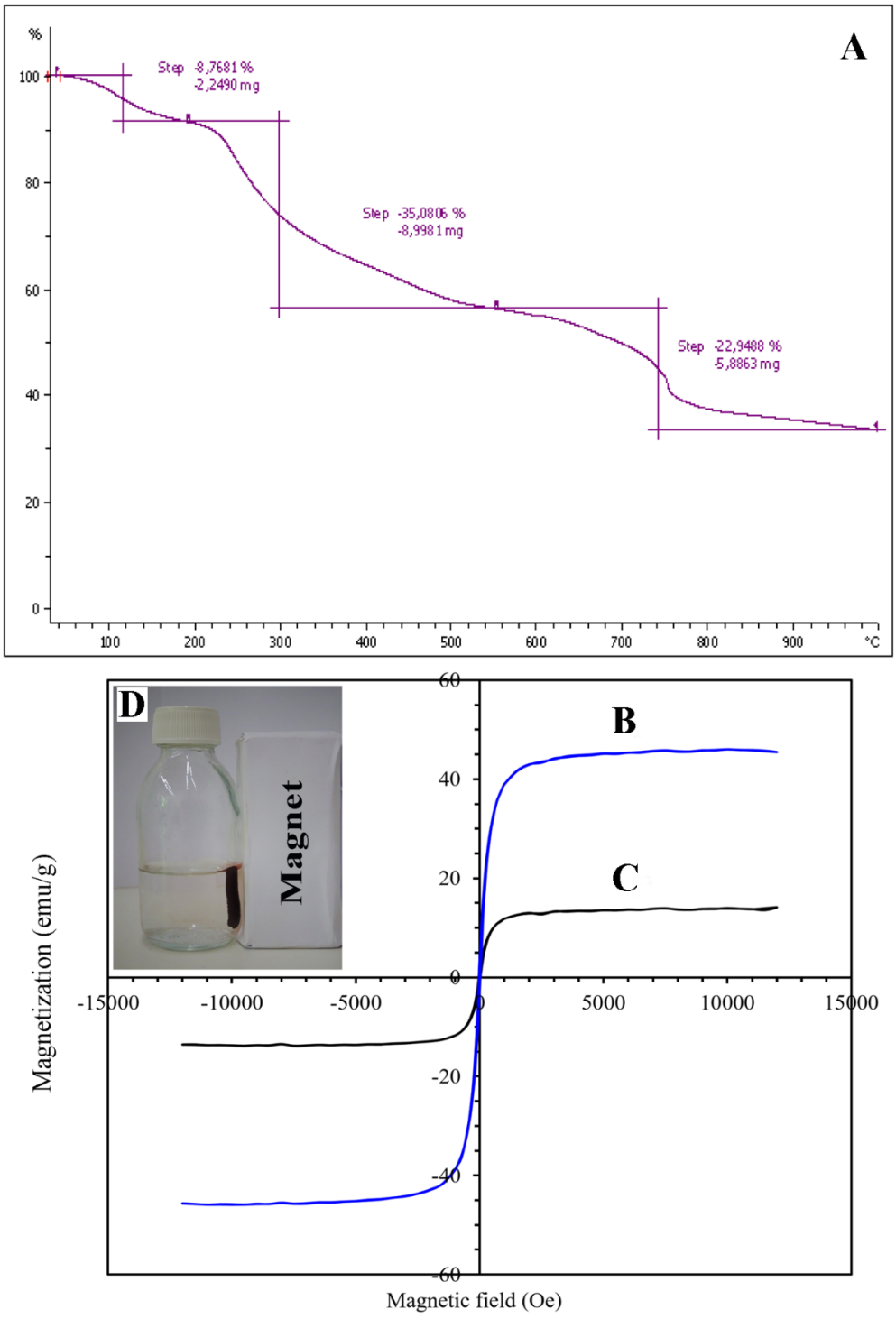

Fig. 5. (A) TGA curve of CA/CMC/$Ni_{0.2}Zn_{0.2}Fe_{2.6}O_4$; Magnetization curves of (B) $Ni_{0.2}Zn_{0.2}Fe_{2.6}O_4$ and (C) CA/CMC/$Ni_{0.2}Zn_{0.2}Fe_{2.6}O_4$; (D) Magnetic separation of the ions-loaded adsorbent.

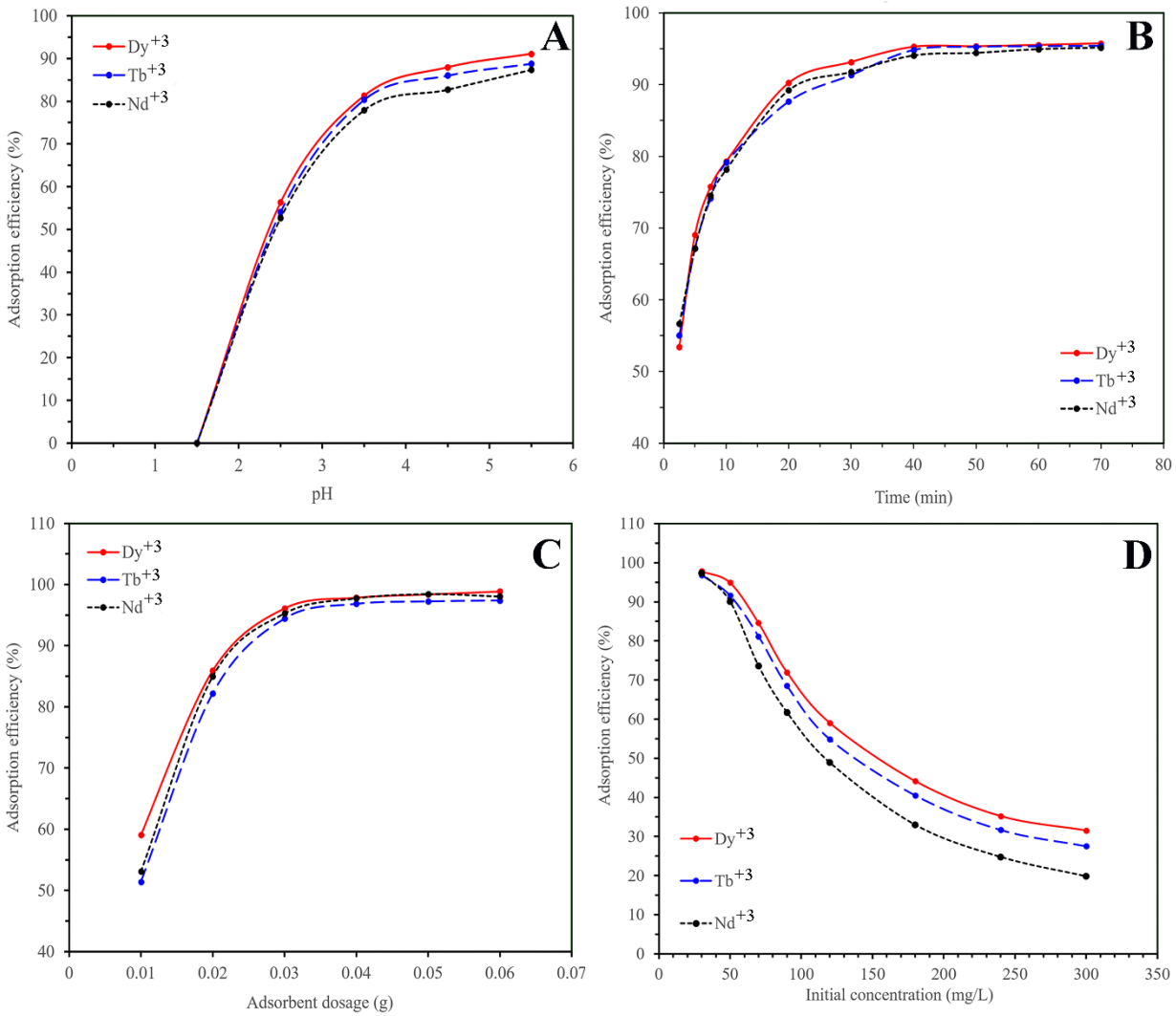

Fig. 6. Effects of (A) pH, (B) contact time, (C) adsorbent dosage, and (D) initial concentration on the adsorption of the ions.

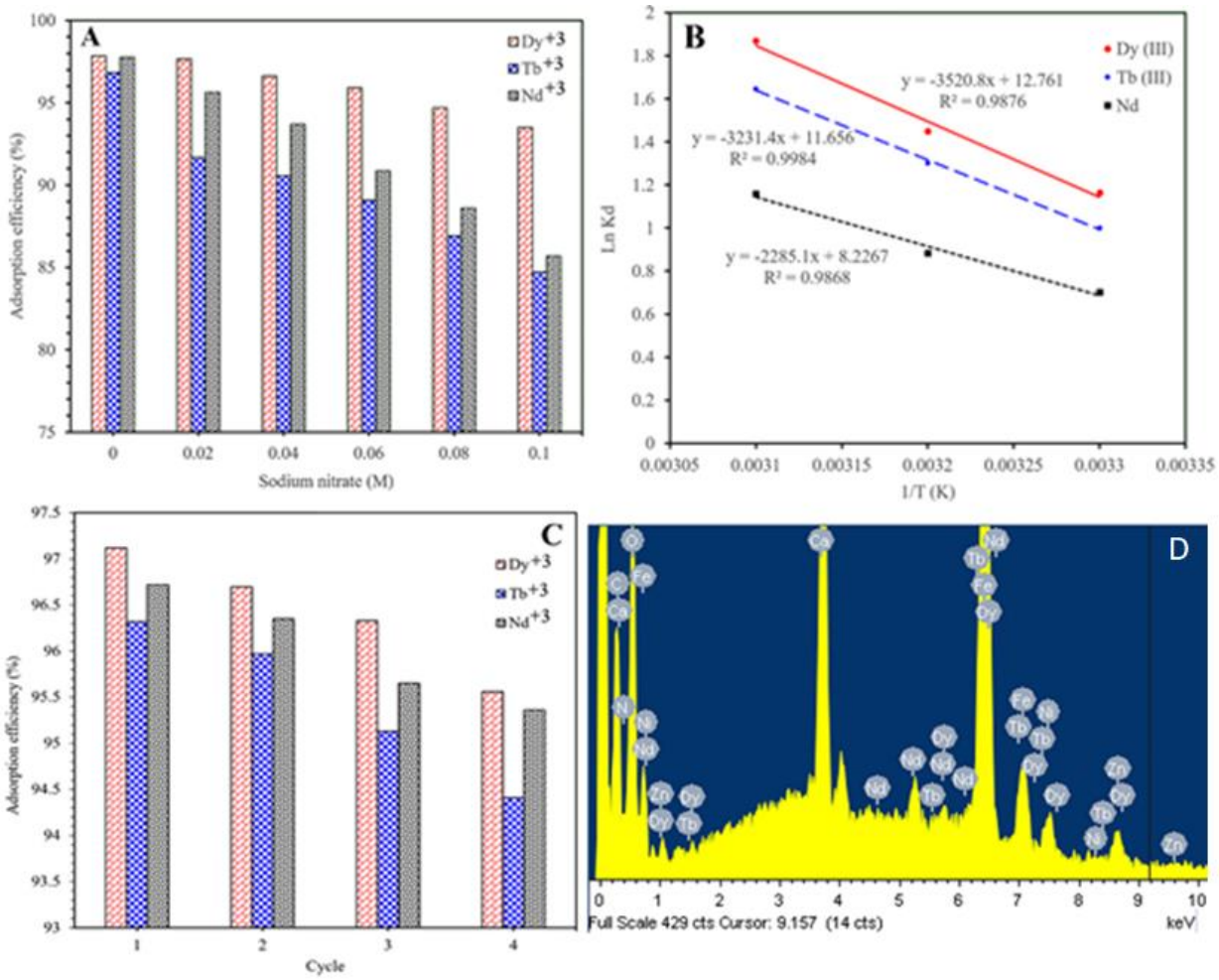

Fig. 7. (A) Effect of ionic strength on the adsorption of Nd^{+3}, Tb^{+3}, and Dy^{+3}, (B) Ln K_d versus 1/T for calculation of enthalpy and entropy changes, (C) Reusability of CA/CMC/$Ni_{0.2}Zn_{0.2}Fe_{2.6}O_4$ for adsorption of the ions, and (D) EDX spectrum of CA/CMC/$Ni_{0.2}Zn_{0.2}Fe_{2.6}O_4$ after adsorption of the ions.

Table 1. Kinetic constants for adsorption of Nd^{+3}, Tb^{+3}, and Dy^{+3} by the CA/CMC/$Ni_{0.2}Zn_{0.2}Fe_{2.6}O_4$.

		Nd^{+3}	Tb^{+3}	Dy^{+3}
PFO	K_1 (1/min)	0.279	0.271	0.269
	q_e (mg/g)	45.91	46.05	46.54
	R^2	0.8506	0.8712	0.9099
	χ^2	7.91	7.29	5.34
PSO	K_2 (g/mg min)	0.00967	0.00916	0.00899
	q_e (mg/g)	48.95	49.21	49.72
	h (mg/g min)	23.17	22.18	22.22
	R^2	0.9831	0.9893	0.9956
	χ^2	0.89	0.60	0.26
IPD	K_i (1/min)	11.33	11.73	11.76
	R^2	0.9063	0.9091	0.8723
	χ^2	4.96	5.14	7.57

Table 2. Isotherm constants for adsorption of Nd^{+3}, Tb^{+3}, and Dy^{+3} by the CA/CMC/$Ni_{0.2}Zn_{0.2}Fe_{2.6}O_4$.

		Nd^{+3}	Tb^{+3}	Dy^{+3}
Langmuir	b (L/mg)	1.075	0.8	0.546
	q_m (mg/g)	73.37	88.61	100.20
	R_L	0.003	0.004	0.006
	R^2	0.9703	0.7163	0.8212
	χ^2	6.04	157.16	144.07
Freundlich	K ($mg^{1-1/n}$ $L^{1/n}$/g)	46.80	46.31	46.65
	n	10.31	6.83	5.93
	R^2	0.8364	0.9905	0.9751
	χ^2	33.32	5.23	20

Table 3. Comparison of the adsorption capacity of Nd^{+3}, Tb^{+3}, and Dy^{+3} onto various adsorbents.

Adsorbent	q_m (mg/g)			Reference
	Nd^{+3}	Tb^{+3}	Dy^{+3}	
Fe_3O_4-C_{18}-chitosan-DETA	27.1		28.3	[41]
EDTA functionalized chitosan	74			[42]
Phosphonic acid functionalized silica microspheres	45			[43]
γ-Fe_2O_3-NH_4OH@SiO_2 (APTMS)			23.2	[44]
Cellulose functionalized with thiourea	73			[45]
MIL-101-PMIDA	70.9			[46]
A layered thiostannate, $(Me_2NH_2)_{1.33}(Me_3NH)_{0.67}Sn_3S_7 \cdot 1.25H_2O$ (FJSM-SnS)	126			[47]
Oxidized multi-walled carbon nanotubes			78.12	[48]
Lanthanide-ion imprinted polymers	126.5			[49]
Macroporous polymeric resin (TVEX-PHOR)		24.93		[50]
TA-MWCNTs		8.55		[51]
PAAm–YZ		42.9		[52]
Poly(acrylamide-expanded perlite) [P(AAm-EP)]		118.3		[53]
P(HEMA–Hap)		109.66		[54]
Poly(amidoxime-hydroxamic acid) resins		125		[55]

CaHAP/NF		130.43		[56]
Acryloyl–phenyl thiourea		74.23		[57]
Hybrid Lewis base ligands functionalized alumina-silica			125.4	[58]
CA@Fe_3O_4 NPs	41			[59]
11-Molybdo-vanadophosphoric acid supported on Zr modified mesoporous silica SBA-15			50	[60]
MPS (22 nm)-2NH-2COOH			44.8	[61]
o-CNCs/GO-IIPs			48.14	[62]
Imprinted mesoporous silica materials			22.33	[63]
CA/CMC/$Ni_{0.2}Zn_{0.2}Fe_{2.6}O_4$	73.37	101.61[a]	114.74[a]	This study

[a] Calculated from Freundlich isotherm

Table 4. Effect of temperature on the adsorption of Nd^{+3}, Tb^{+3}, and Dy^{+3} at 90 mg/L and thermodynamic parameters.

	Adsorption efficiency (%)		
Temperature (^{o}C)	Nd^{+3}	Tb^{+3}	Dy^{+3}
25	61.72	68.51	71.95
35	65.95	74.61	77.31
45	71.81	80.59	83.84
Thermodynamic parameters			

		Nd^{+3}	Tb^{+3}	Dy^{+3}
ΔH° (kJ/mol)		19.00	26.86	29.27
ΔS° (kJ/mol K)		0.068	0.097	0.106
	Temperature ($^{\circ}C$)			
	25	-1.737	-2.478	-2.887
ΔG° (kJ/mol)	35	-2.263	-3.331	-3.71
	45	-3.062	-4.353	-4.943

Higlights

- The magnetic calcium alginate/carboxymethyl chitosan bionanocomposite was prepared.
- The saturation magnetization of the product was 14.14 emu/g.
- Nd (III), Tb (III), and Dy (III) adsorption was investigated.
- The adsorption kinetic data were fitted with pseudo-second-order model.

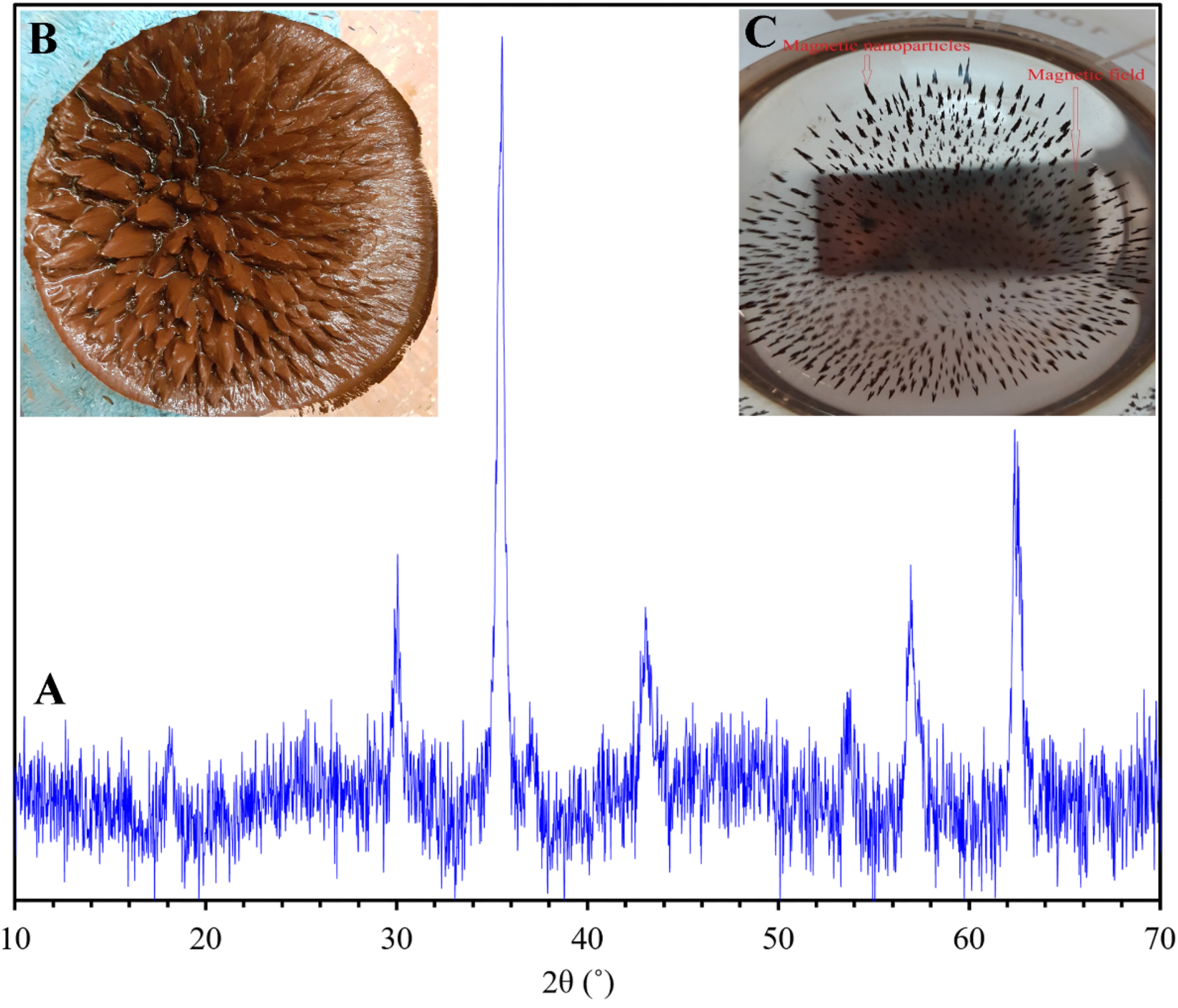
B
C
Magnetic nanoparticles
Magnetic field
A
10
20
30
40
50
60
70
2θ (°)

Figure 1

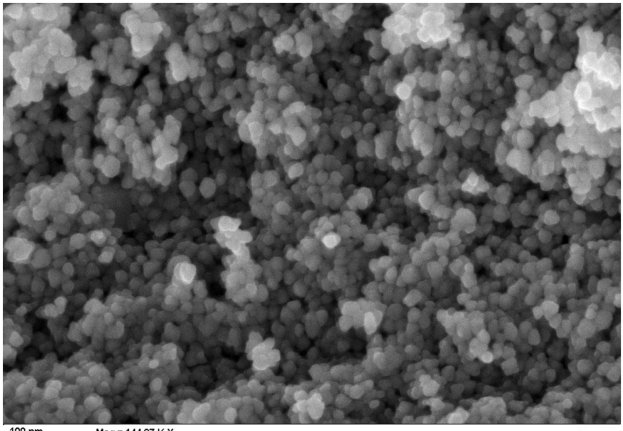
100 nm
Mag = 144.87 K X
WD = 4.6 mm
EHT = 5.00 kV

A

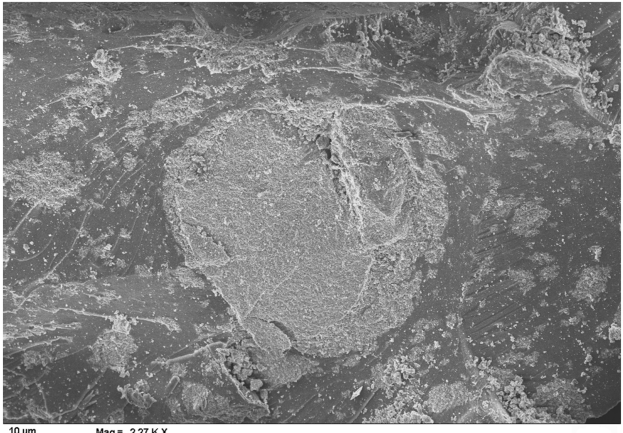
10 µm
Mag = 2.27 K X
WD = 3.8 mm
EHT = 5.00 kV

B

Figure 2

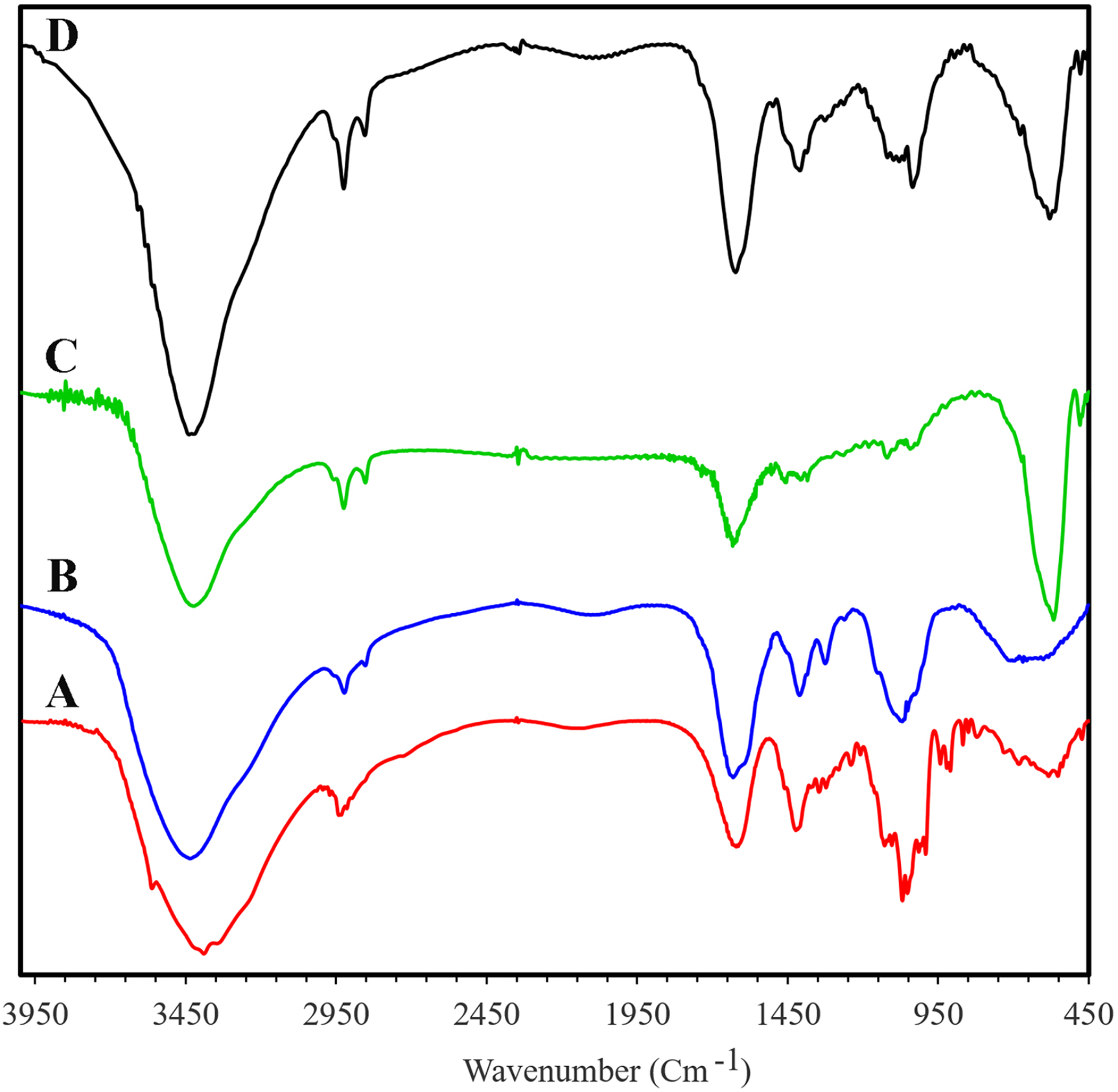

Figure 3

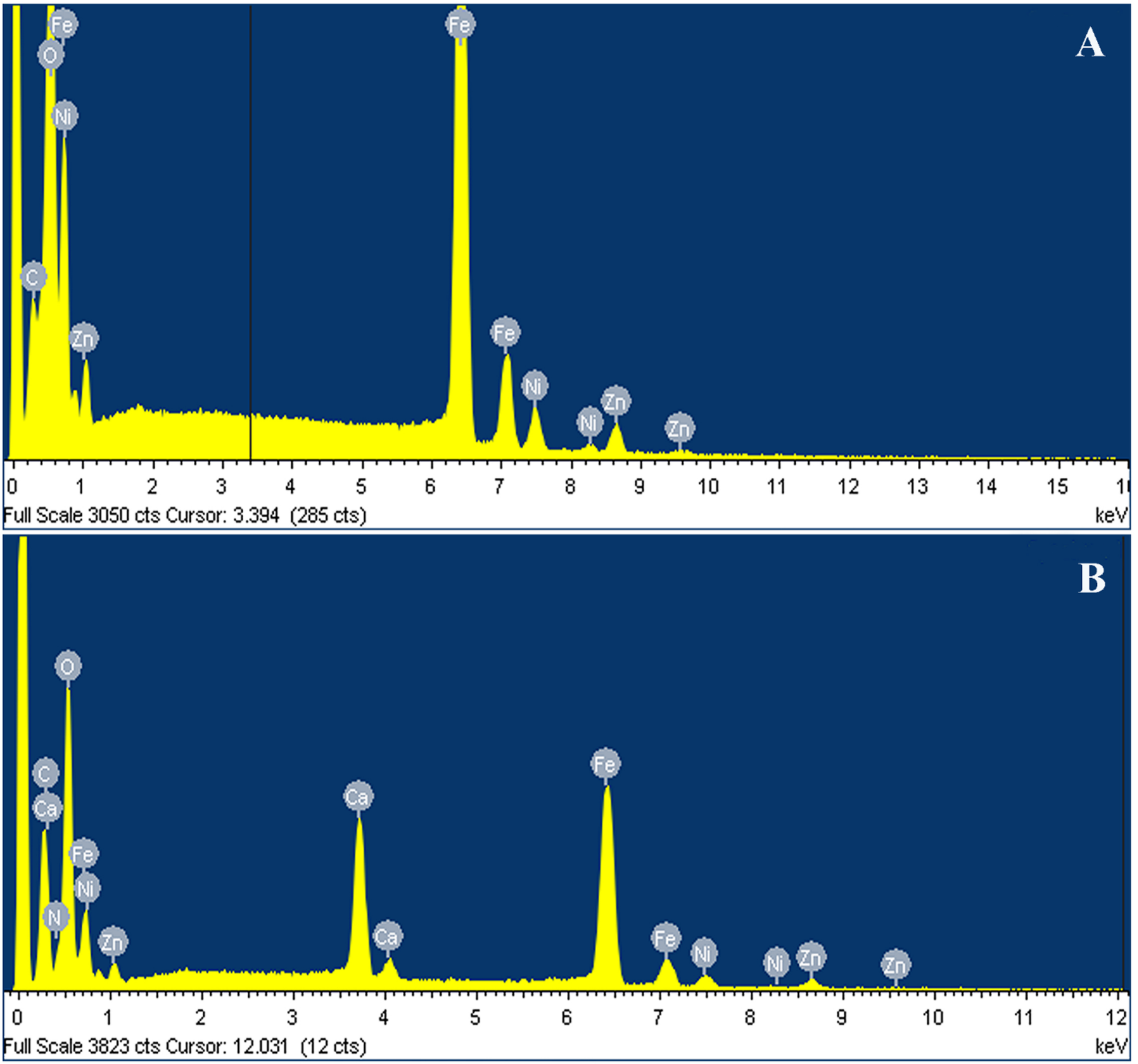
A
Fe
O
Ni
C
Zn
Fe
Fe
Ni
Ni
Zn
Zn
0 1 2 3 4 5 6 7 8 9 10 11 12 13 14 15
Full Scale 3050 cts Cursor: 3.394 (285 cts)
keV
B
O
C
Ca
Fe
Ni
N
Zn
Ca
Ca
Fe
Fe
Ni
Ni
Zn
Zn
0 1 2 3 4 5 6 7 8 9 10 11 12
Full Scale 3823 cts Cursor: 12.031 (12 cts)
keV

Figure 4

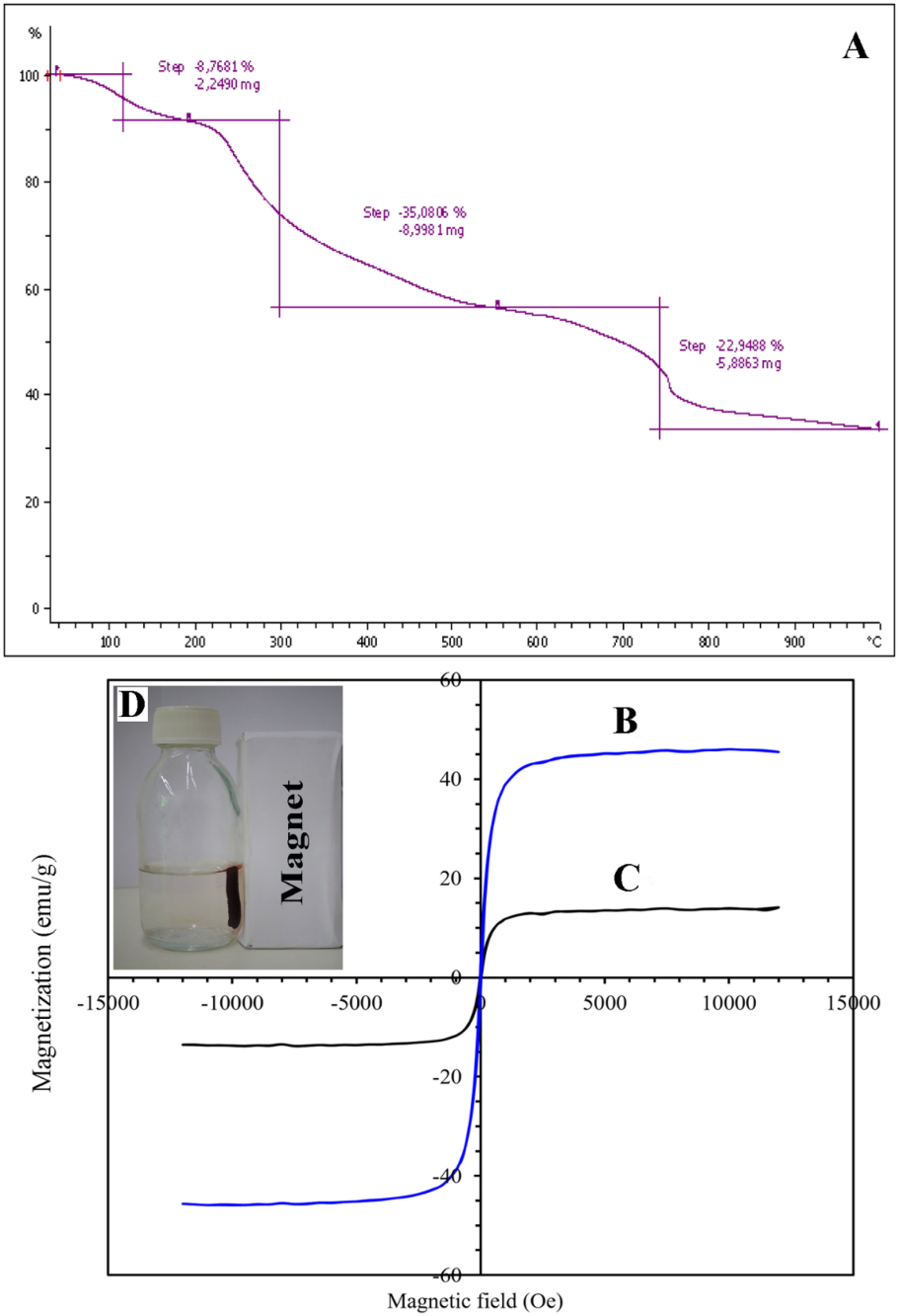
A
%
Step -8,7681 %
-2,2490 mg
Step -35,0806 %
-8,9981 mg
Step -22,9488 %
-5,8863 mg
°C
D
Magnet
B
C
Magnetization (emu/g)
Magnetic field (Oe)

Figure 5

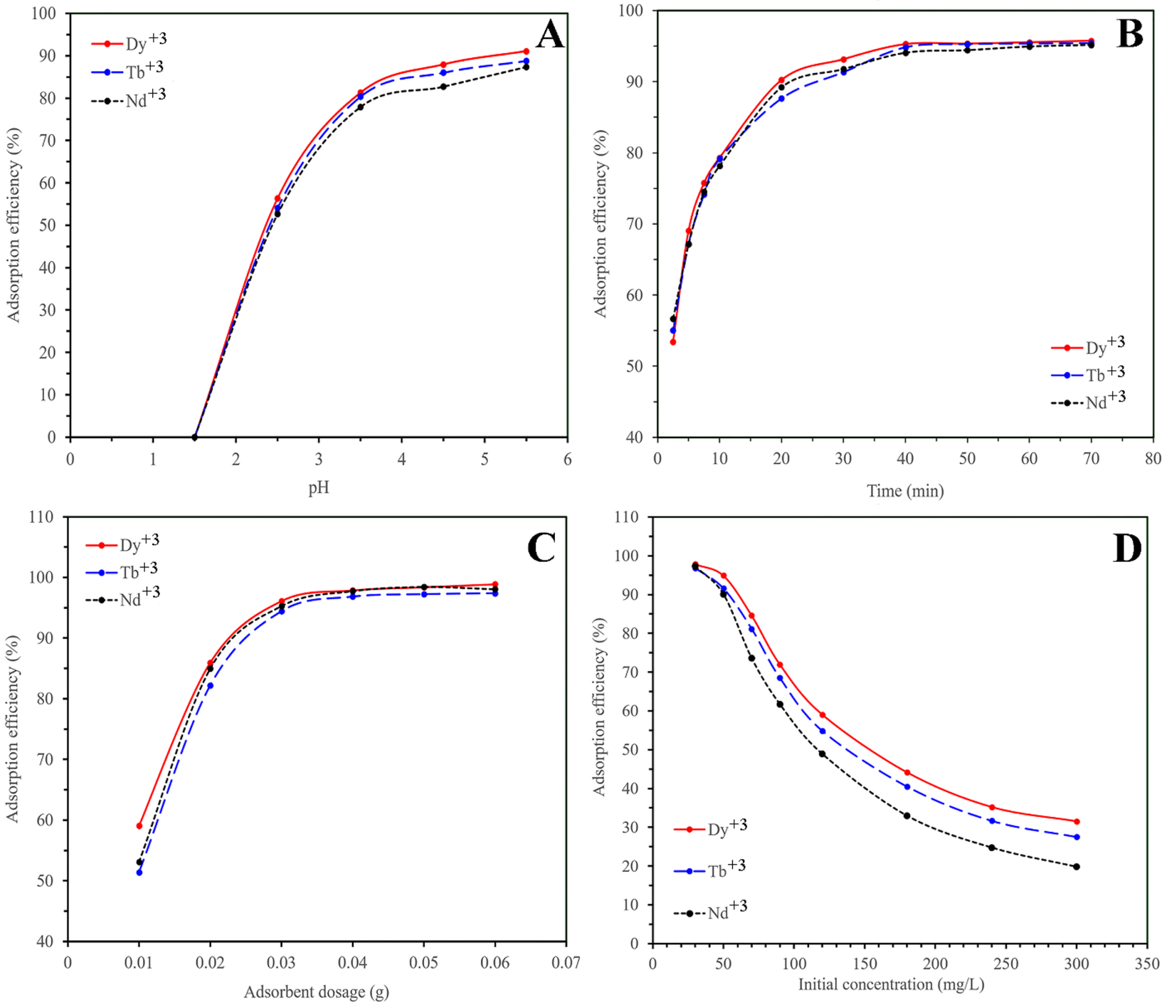
A
Dy+3
Tb+3
Nd+3
Adsorption efficiency (%)
pH
B
Time (min)
C
Adsorbent dosage (g)
D
Initial concentration (mg/L)

Figure 6

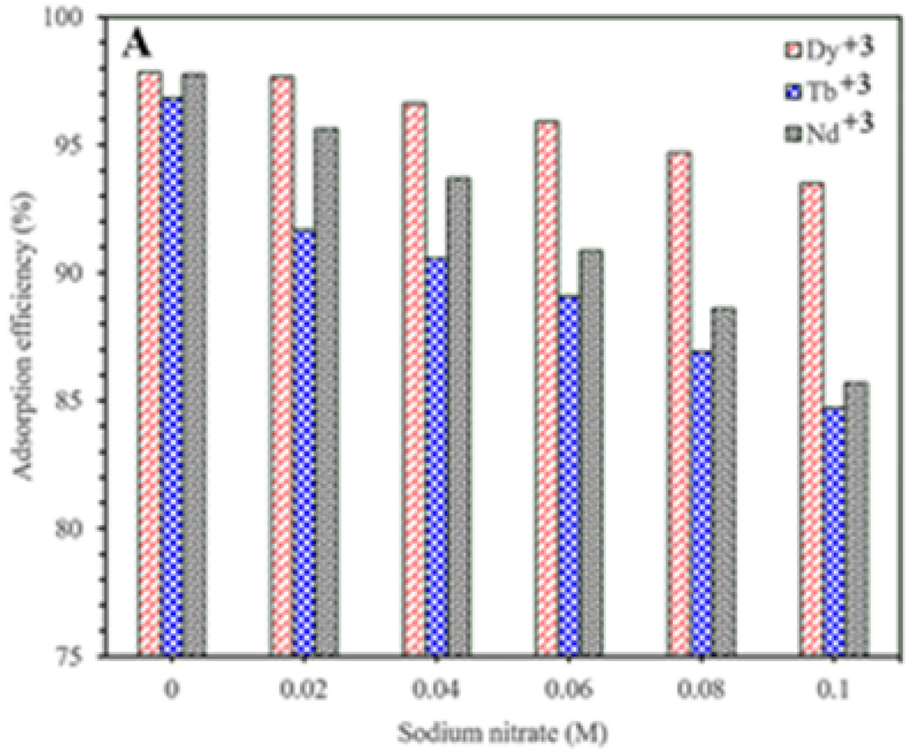
A
Dy+3
Tb+3
Nd+3
Adsorption efficiency (%)
Sodium nitrate (M)

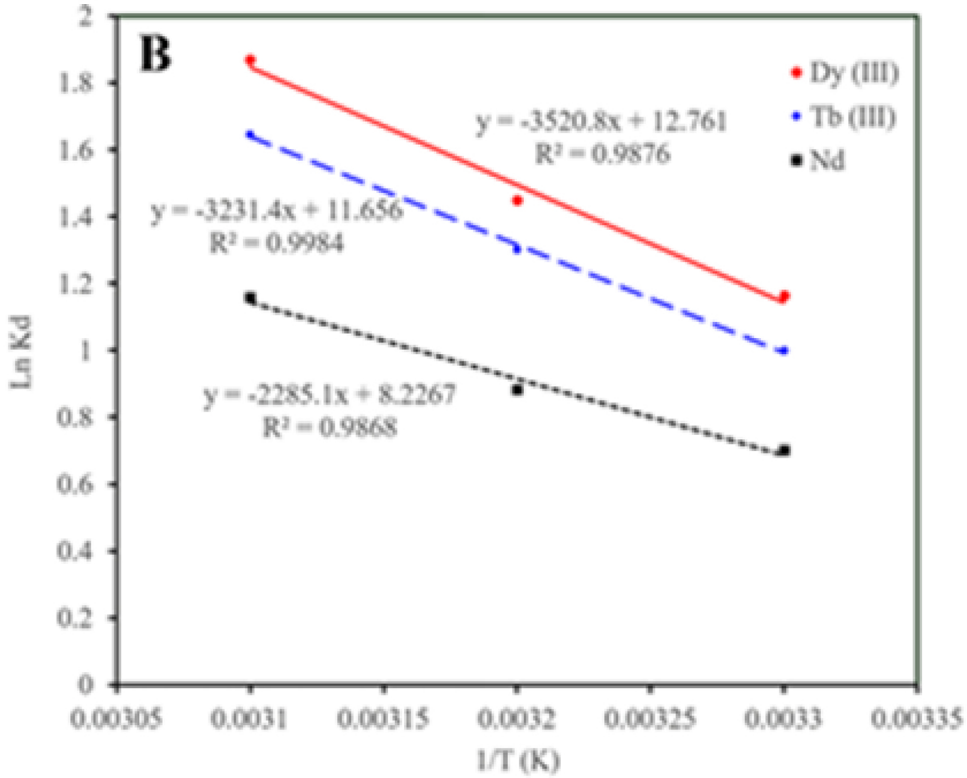
B
Dy (III)
Tb (III)
Nd
y = -3520.8x + 12.761
R² = 0.9876
y = -3231.4x + 11.656
R² = 0.9984
y = -2285.1x + 8.2267
R² = 0.9868
Ln Kd
1/T (K)

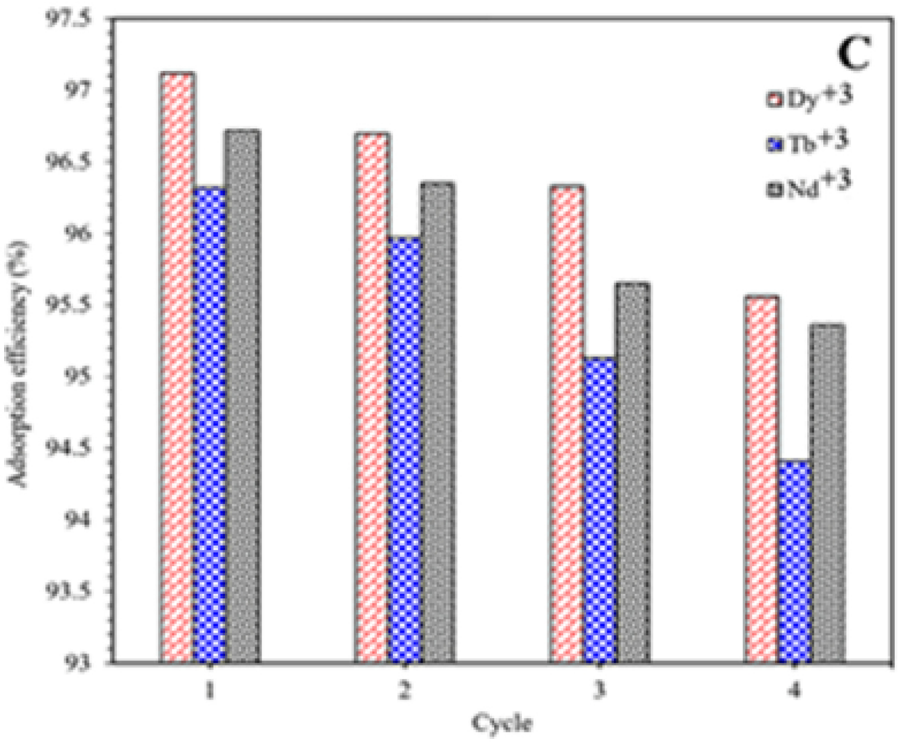
C
Dy+3
Tb+3
Nd+3
Adsorption efficiency (%)
Cycle

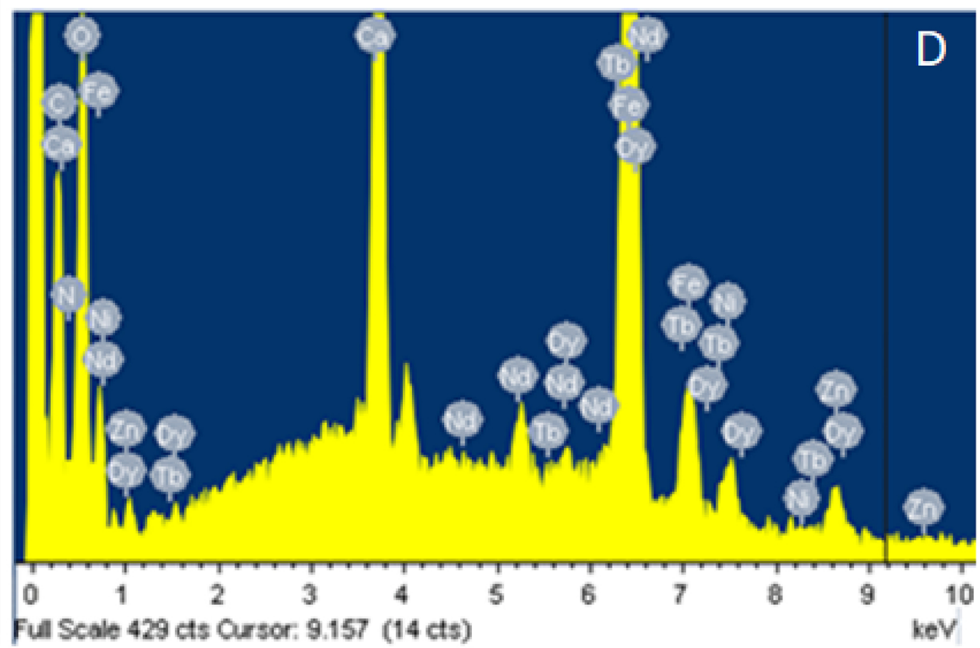
D
Full Scale 429 cts Cursor: 9.157 (14 cts)
keV

Figure 7